

## REVIEW

[View Article Online](#)  
[View Journal](#) | [View Issue](#)Cite this: *J. Mater. Chem. A*, 2022, 10, 5792Advances in studies of the structural effects of supported Ni catalysts for CO<sub>2</sub> hydrogenation: from nanoparticle to single atom catalystZhitao Zhang,<sup>a</sup> Chenyang Shen,<sup>a</sup> Kaihang Sun,<sup>a</sup> Xinyu Jia,<sup>a</sup> Jingyun Ye <sup>\*b</sup> and Chang-jun Liu <sup>\*a</sup>

Supported Ni catalysts are promising for CO<sub>2</sub> hydrogenation because of their relatively cheap price with comparable activity to noble metal catalysts. The product of CO<sub>2</sub> hydrogenation over a supported Ni catalyst can theoretically be methane, CO, methanol and formic acid. The electronic and geometric structures of a supported Ni catalyst have a significant effect on the activity and selectivity of CO<sub>2</sub> hydrogenation. Supported single nickel atom catalysts are found to tend to form carbon monoxide, methanol and, theoretically, formic acid. The selectivity depends on the support. The supported nickel cluster on indium oxide and In<sub>2</sub>O<sub>3</sub>–ZrO<sub>2</sub> is highly selective for methanol synthesis. Supported nickel nanoparticles are normally good catalysts for methane formation at reasonably low temperatures. However, the structural effect of the supported Ni catalyst on CO<sub>2</sub> hydrogenation has not been well investigated. The mechanism is still in debate. To further improve the activity and stability with tunable selectivity, the structure control of the Ni catalyst is very necessary for CO<sub>2</sub> hydrogenation, which is highly structure sensitive. In this review, recent advances in the understanding of the structural effects of supported Ni catalysts on CO<sub>2</sub> hydrogenation are summarized, including theoretical studies, *operando* or *in situ* catalyst characterization and experimental studies. Future development is therefore finally addressed.

Received 19th November 2021  
Accepted 1st February 2022

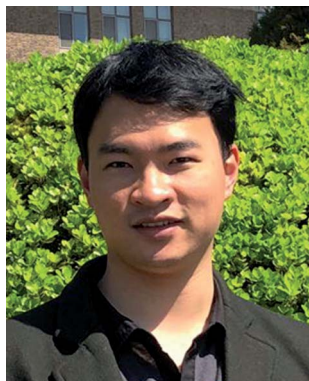
DOI: 10.1039/d1ta09914k

[rsc.li/materials-a](https://rsc.li/materials-a)

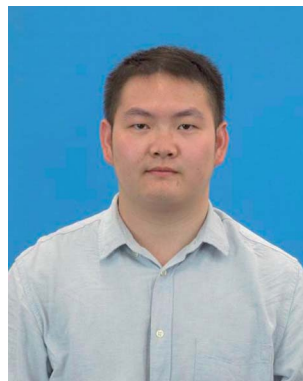
## 1. Introduction

With the rapid development of renewable energy, the heterogeneous hydrogenation of carbon dioxide (CO<sub>2</sub>) has attracted

significantly increasing attention worldwide owing to its potential in large scale utilization of carbon dioxide.<sup>1–4</sup> CO<sub>2</sub> hydrogenation has also been considered to be promising for energy storage.<sup>5–7</sup> Many catalysts have been exploited and reported for CO<sub>2</sub> hydrogenation.<sup>8–22</sup> Among all the catalysts exploited, supported nickel catalysts are promising because of their high activity and relatively low price.<sup>8–15</sup> In addition, supported nickel catalysts have been employed in the industrial

<sup>a</sup>School of Chemical Engineering and Technology, Tianjin University, Tianjin, 300072, China. E-mail: [cjL@tju.edu.cn](mailto:cjL@tju.edu.cn)<sup>b</sup>Department of Chemistry and Biomolecular Science, Clarkson University, Potsdam, New York 13699, USA. E-mail: [jingyun.ye324@gmail.com](mailto:jingyun.ye324@gmail.com)

Zhitao Zhang is currently a PhD candidate in the School of Chemical Engineering and Technology at Tianjin University, China. His research topic is the preparation and characterization of supported nickel catalysts for CO<sub>2</sub> hydrogenation and the desulfurization of gaseous hydrocarbons. He has published two papers in *Catalysis Communications* and *Chinese Chemical Letters* and co-authored four other papers.



Chenyang Shen is currently a PhD candidate in the School of Chemical Engineering and Technology at Tianjin University, China. His research topic is the theoretical and experimental studies of supported nickel and iridium catalysts for CO<sub>2</sub> hydrogenation. He has published two papers in *ACS Catalysis* and *Journal of Energy Chemistry* and co-authored eight other papers.

production of syngas (CO and hydrogen) *via* steam reforming of methane, a reverse reaction of CO<sub>2</sub> hydrogenation to methane, which is normally called CO<sub>2</sub> methanation and well-known as the Sabatier reaction.<sup>3,21</sup> Theoretically, the product of CO<sub>2</sub> hydrogenation over a supported nickel catalyst can be methane, methanol, carbon monoxide through the reverse water gas shift (RWGS) reaction, and formic acid. Methanol, formic acid and carbon monoxide are important intermediates for syntheses of various chemicals. Methanol can be directly used as fuel. CO<sub>2</sub> methanation has potential applications in clean fuel production, energy storage, carbon recycling and water supply for spacecraft.<sup>23</sup> Formic acid has been used for disinfection.<sup>24</sup> It can

be used to produce hydrogen for fuel cell applications<sup>24,25</sup> because of its high hydrogen content (53 g L<sup>-1</sup>; 4.4 wt%).<sup>24</sup>

The activity, selectivity and stability of supported Ni catalysts basically depend upon the electronic and geometric structures of the catalyst. A change in the electronic structure can cause a big change in the selectivity.<sup>26–35</sup> One can shift the selectivity of CO<sub>2</sub> hydrogenation from selective production of methane to methanol or CO or even formic acid by the change of the catalyst structure. The electronic structure of a supported Ni catalyst can be tuned by the physical structure and components, including the supporting material, of the catalyst. The size control of nickel catalysts is an effective approach to affect the geometric and electronic structures of the catalyst. The strong nickel-support



*Kaihang Sun is currently a PhD candidate in the School of Chemical Engineering and Technology at Tianjin University, China. His research topic is the theoretical and experimental studies of supported Ni, Pt and Ag catalysts for CO<sub>2</sub> hydrogenation. He published the first pioneering experimental work on In<sub>2</sub>O<sub>3</sub> for CO<sub>2</sub> hydrogenation to methanol. He published another three papers in Green Chem-*

*istry, Green Energy & Environment and Journal of Physical Chemistry C and co-authored seven other papers.*



*Jingyun Ye is currently an Assistant Professor in the Department of Chemistry of Clarkson University. She obtained her PhD degree from Tianjin University in 2014. After that, she was a postdoctoral researcher at the University of Pittsburgh and the University of Minnesota before she joined Clarkson University in 2020. She carried out the pioneering theoretical study of In<sub>2</sub>O<sub>3</sub> for CO<sub>2</sub>*

*hydrogenation to methanol and initiated the new research topic on In<sub>2</sub>O<sub>3</sub> based catalysts for CO<sub>2</sub> hydrogenation. She is also one of the first scientists who worked on MOF based heterogeneous catalysts. Her research interest is to precisely design multi-functional materials and efficient catalysts for sustainable energy conversion and storage. She has published papers in Journal of the American Chemical Society, ACS Catalysis, Applied Catalysis B: Environmental, Journal of Catalysis, ChemCatChem, Catalysis Science & Technology, ChemComm, Journal of Physical Chemistry C and others.*



*Xinyu Jia, a former PhD student of Tianjin University, is currently a lecturer at the Xi'an University of Science & Technology, China. Her research topic is the experimental studies of supported nickel catalysts for CO<sub>2</sub> hydrogenation. She invented the Ni/In<sub>2</sub>O<sub>3</sub> catalyst for CO<sub>2</sub> hydrogenation to methanol. She has published three papers in Applied Catalysis B, Catalysis Today and Journal of Energy*

*Chemistry and co-authored four other papers.*



*Chang-jun Liu is a Chang Jiang Distinguished Professor and Fellow of the Royal Society of Chemistry. His research interests include CO<sub>2</sub> utilization, natural gas conversion, plasma nanoscience, and 3D printing. He has been in the list of highly cited Chinese authors (Chemical Engineering) by Elsevier since 2014. He served as the 2010 Program Chair of Fuel Chemistry Division of American Chemical Society*

*and Chair of the 10<sup>th</sup> International Conference on CO<sub>2</sub> Utilization. He is in the editorial board of Applied Catalysis B, Journal of CO<sub>2</sub> Utilization and Chinese Journal of Catalysis. He is in the advisory board of Greenhouse Gases: Science & Technology.*

interaction with the reducible oxides can be employed to adjust the electronic structure of the supported nickel catalyst. This can not only improve the catalytic activity but can also totally change the selectivity of the product of CO<sub>2</sub> hydrogenation.

According to a literature survey, most reported studies of CO<sub>2</sub> hydrogenation on supported Ni catalysts are for methane synthesis. With increasing studies on nickel cluster or single nickel atom catalysts (Ni-SACs), CO<sub>2</sub> hydrogenation to methanol or formic acid attracts more and more interest. More progress can be expected for CO<sub>2</sub> hydrogenation to methanol or formic acid over the supported nickel catalyst. Owing to the big changes in the electronic structures from nickel nanoparticles (NPs) to Ni-SACs, CO<sub>2</sub> hydrogenation over the supported nickel catalyst is excellent for the study of structural effects on the catalytic properties. The supported Ni-SAC has much higher accessibility of all nickel atoms to CO<sub>2</sub> and hydrogen. It can be an excellent connection between a homogeneous catalyst, with a well-defined structure, and a heterogeneous catalyst, which can be easily separated after the reaction with low cost both in the material and reaction operation for large scale applications.

We have to acknowledge that the structural effect of Ni catalysts on CO<sub>2</sub> hydrogenation is complex. It has not been well investigated because the structure of the nickel catalyst is subject to dynamic changes with the involvement of the oxide support, various active sites and adsorbates of different reactivities during the reaction. The reaction mechanism with structure evolution is still in debate. In this review, we attempt to summarize recent advances in the studies of structural effects of supported Ni catalysts on CO<sub>2</sub> hydrogenation to methane, carbon monoxide and methanol. CO<sub>2</sub> hydrogenation to formic acid on a supported nickel catalyst only showed the theoretical possibility at present. We will briefly mention it during discussions on related issues. We focus on the theoretical understanding, *operando* study or *in situ* catalyst characterization and the structure–activity relationship, *via* the size effect (from nickel nanoparticles to Ni-SAC), of the supported

nickel catalyst for heterogeneous CO<sub>2</sub> hydrogenation thermally. However, the discussions here are helpful for the design and preparation of supported nickel catalysts for photo-catalytic, photo-thermal-catalytic and electro-catalytic reduction of CO<sub>2</sub>. Future developments are addressed finally.

## 2. Reactions in CO<sub>2</sub> hydrogenation

The characteristics of CO<sub>2</sub> molecules and the thermodynamic aspects of CO<sub>2</sub> hydrogenation have been well discussed in review articles.<sup>8–20</sup> Theoretically, CO<sub>2</sub> hydrogenation can produce carbon monoxide, methane, methanol and formic acid,<sup>10,11</sup> as shown in Table 1. Thermodynamically, CO<sub>2</sub> methanation (reaction (4) in Table 1) is highly favoured ( $\Delta G_{298K}^\circ = -132.4$  kJ mol<sup>-1</sup>). It has to be carried out at moderately low temperatures to limit the competitive endothermal RWGS reaction. This means that CO production from CO<sub>2</sub> hydrogenation is normally carried out at elevated temperatures.<sup>11,36,37</sup> A significant challenge is to improve the catalytic activity of CO<sub>2</sub> methanation at low temperatures. CO<sub>2</sub> hydrogenation to methanol (reaction (2) in Table 1) is also thermodynamically favoured ( $\Delta G_{298K}^\circ = -10.7$  kJ mol<sup>-1</sup>) and exothermic. It has to be carried out at moderately low temperatures as well to avoid the reverse reaction and to inhibit the side RWGS reaction. CO<sub>2</sub> hydrogenation to formic acid (reactions (7) and (8) in Table 1) is a little thermodynamically difficult. The catalyst for this reaction needs the aid of alkaline aqueous solution<sup>24</sup> or unique support additives.<sup>32,33</sup>

Prof. Chen and his co-workers presented a reaction network for CO<sub>2</sub> hydrogenation to CO, CH<sub>3</sub>OH and CH<sub>4</sub>.<sup>10,15</sup> This reaction network can be further modified based on our recent DFT studies of CO<sub>2</sub> hydrogenation to methanol.<sup>22</sup> Fig. 1 shows the modified reaction network,<sup>22</sup> which includes CO<sub>2</sub> hydrogenation to formic acid *via* the formate route (right green path).

As seen in Fig. 1, a complex reaction network exists with various chemical intermediates on the catalyst. Methane, CO

Table 1 The major reactions in CO<sub>2</sub> hydrogenation

| No. | Reaction  | $\Delta H_{298K}^\circ$ (kJ mol <sup>-1</sup> ) | $\Delta G_{298K}^\circ$ (kJ mol <sup>-1</sup> ) |
|-----|---|---|---|
| 1   | CO <sub>2</sub> + 3H <sub>2</sub> ⇌ CH <sub>3</sub> OH(g) + H <sub>2</sub> O(g) | −49.3   | +3.5  |
| 2   | CO <sub>2</sub> + 3H <sub>2</sub> ⇌ CH <sub>3</sub> OH(l) + H <sub>2</sub> O(l) | −137.8  | −10.7   |
| 3   | CO <sub>2</sub> + 4H <sub>2</sub> ⇌ CH <sub>4</sub> + 2H <sub>2</sub> O(g)      | −165.0  | −113.5  |
| 4   | CO <sub>2</sub> + 4H <sub>2</sub> ⇌ CH <sub>4</sub> + 2H <sub>2</sub> O(l)      | −259.9  | −132.4  |
| 5   | CO <sub>2</sub> + H <sub>2</sub> ⇌ CO + H <sub>2</sub> O(g)                     | +41.2   | +28.6   |
| 6   | CO <sub>2</sub> + H <sub>2</sub> ⇌ CO + H <sub>2</sub> O(l)                     | −6.2  | +19.2   |
| 7   | CO <sub>2</sub> + H <sub>2</sub> ⇌ HCOOH(g)                                     | +43.5   | +14.9   |
| 8   | CO <sub>2</sub> + H <sub>2</sub> ⇌ HCOOH(l)                                     | −31.0   | +34.3   |
| 9   | CO + 2H <sub>2</sub> ⇌ CH <sub>3</sub> OH(g)                                    | −90.6   | −29.1   |
| 10  | CO + 2H <sub>2</sub> ⇌ CH <sub>3</sub> OH(l)                                    | −131.6  | −29.9   |
| 11  | CO + 3H <sub>2</sub> ⇌ CH <sub>4</sub> + H <sub>2</sub> O(g)                    | −206.1  | −141.8  |
| 12  | CO + 3H <sub>2</sub> ⇌ CH <sub>4</sub> + H <sub>2</sub> O(l)                    | −229.7  | −165.1  |
| 13  | 2CO + 2H <sub>2</sub> ⇌ CH <sub>4</sub> + CO <sub>2</sub>                       | −247.3  | −170.4  |
| 14  | CH <sub>4</sub> ⇌ C(s) + 2H <sub>2</sub>  | +74.8   | +50.7   |
| 15  | 2CO ⇌ C(s) + CO <sub>2</sub>  | −172.4  | −119.7  |
| 16  | CO + H <sub>2</sub> ⇌ C(s) + H <sub>2</sub> O(g)                                | −131.3  | −91.1   |
| 17  | CO + H <sub>2</sub> ⇌ C(s) + H <sub>2</sub> O(l)                                | −178.7  | −100.7  |
| 18  | CO <sub>2</sub> + 2H <sub>2</sub> ⇌ C(s) + 2H <sub>2</sub> O(g)                 | −90.1   | −62.5   |

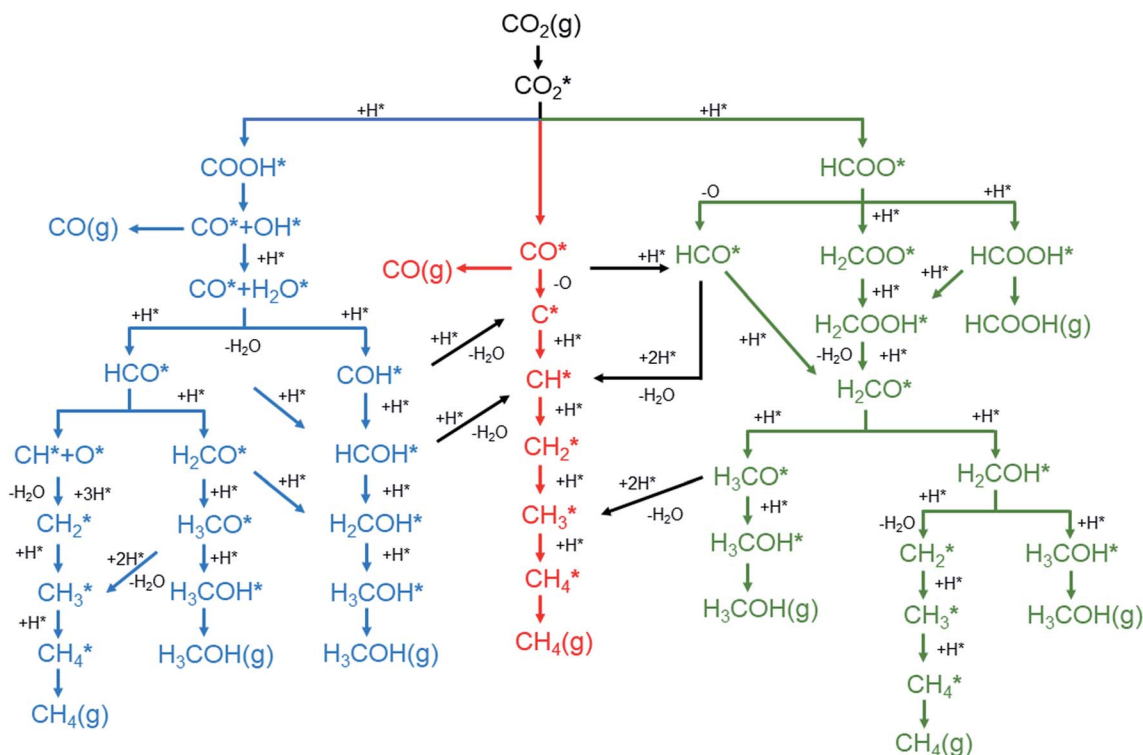


Fig. 1 The modified reaction network of CO<sub>2</sub> hydrogenation over the supported nickel catalysts.<sup>22</sup> (\* means the adsorbed species). Copyright 2022, Elsevier.

and methanol can be obtained from multiple routes. Two general pathways are derived from CO<sub>2</sub> dissociation. One is the direct CO<sub>2</sub> dissociation *via* the redox mechanism (CO<sub>2</sub>\* → CO\* + O\*, red paths). The other is the hydrogen-assisted CO<sub>2</sub> dissociation, as shown in Fig. 1, either *via* formate (CO<sub>2</sub>\* + H\* → HCOO\*, green paths) or carboxylate (CO<sub>2</sub>\* + H\* → COOH\*, blue paths) intermediates, while H\* is from H<sub>2</sub> dissociation (H<sub>2</sub> → H\* + H\*). The exact route principally depends on the catalyst structure.

### 3. CO<sub>2</sub> adsorption

The adsorption and activation of CO<sub>2</sub> on the nickel surface play an important role in CO<sub>2</sub> hydrogenation. The formation of adsorbed CO<sub>2</sub> from gas phase CO<sub>2</sub> can be the largest barrier for the dissociation of CO<sub>2</sub>(g).<sup>38</sup> Two mechanisms for CO<sub>2</sub> adsorption on the Ni catalyst exist. One is the dissociative adsorption (CO<sub>2</sub>\* → CO\* + C\*). The other is the non-dissociative adsorption (CO<sub>2</sub> + δe<sup>-</sup> → CO<sub>2</sub><sup>δ-</sup>) to form a bent CO<sub>2</sub><sup>δ-</sup> structural mode from the nickel to CO<sub>2</sub> charge transfer.<sup>39</sup> The ability of CO<sub>2</sub> chemisorption on Ni surfaces was found in the order of Ni (211) > Ni (110) > Ni (100) > Ni (111), as shown in Table 2.<sup>40–50</sup> The higher CO<sub>2</sub> adsorption energies on the stepped Ni (211) was attributed to the stronger charge transfer on Ni (211) than on other low index surfaces.<sup>41</sup> The results suggest that low coordinated Ni surfaces are more active for CO<sub>2</sub> chemisorption with their stronger ability of electron donation. This also explains that smaller Ni clusters show stronger CO<sub>2</sub> adsorption ability.

For example, the CO<sub>2</sub> adsorption energy on Ni<sub>13</sub> is −1.25 eV (ref. 51) or −120.2 kJ mol<sup>-1</sup> (ref. 51) and −100 kJ mol<sup>-1</sup>,<sup>52</sup> while it is −58 kJ mol<sup>-1</sup> on Ni<sub>55</sub>.<sup>52</sup> These suggest that CO<sub>2</sub> adsorption can be enhanced by increasing the defects (*e.g.*, steps, edges, corners and doping with second metal atoms) of the Ni surfaces or decreasing the size of Ni nanoparticles.

The support material has a significant effect on CO<sub>2</sub> adsorption over a Ni catalyst.<sup>22,53–55</sup> It depends on the interaction between nickel and the support. The loading of Ni clusters on yttria-stabilized zirconia (YSZ) can increase the CO<sub>2</sub> adsorption energy from −0.37 eV on YSZ(111) to −1.16 eV on Ni<sub>4</sub>/YSZ(111).<sup>54</sup> The nickel loading on CeO<sub>2</sub>(111) also causes an increase of the CO<sub>2</sub> adsorption energy from −0.27 eV (CeO<sub>2</sub>(111)) to −0.79 eV (Ni/CeO<sub>2</sub>(111)).<sup>55</sup> CO<sub>2</sub> can be stabilized at the interface of the Ni clusters and CeO<sub>2</sub> surface. The oxygen vacancy in CeO<sub>2</sub> plays an important role with it.<sup>55</sup> The oxygen vacancy has significant effects on the electronic structure and the properties of the Ni catalyst on the reducible oxide support, like CeO<sub>2</sub> (ref. 55) and In<sub>2</sub>O<sub>3</sub>.<sup>22</sup> The CO<sub>2</sub> adsorption energy is −0.66 eV for Ni<sub>4</sub>/In<sub>2</sub>O<sub>3</sub> with an oxygen vacancy, which it is −0.43 eV for the catalyst without an oxygen vacancy.<sup>22</sup>

The size of the nickel cluster on the support has a significant effect as well.<sup>54</sup> If the nickel catalyst size is reduced to a SAC, CO<sub>2</sub> dissociative adsorption on CeO<sub>2</sub> supported Ni<sub>1</sub> becomes difficult with a Gibbs free energy change of 0.76 eV, even in the presence of an oxygen vacancy.<sup>56</sup> Alonso *et al.*<sup>57</sup> found that a Ni-SAC, supported by MFI zeolite, adsorbs CO<sub>2</sub> so strongly that CO<sub>2</sub> cannot be dissociated to CO\* and O\*. It could hydrogenate CO<sub>2</sub>



**Table 2** Adsorption energies ( $E_{\text{ads}}$ ) of  $\text{CO}_2$  and CO on the most stable sites on the Ni (111), (100), (110) and (211) surfaces

| $E_{\text{ads}}$ (eV) | $\text{CO}_2^*$       | $\text{CO}^*$         | Ref.            |
|-----------------------|-----------------------|-----------------------|-----------------|
| Ni (111)              | 0.26 ( $q = -0.45$ )  | -1.91 ( $q = -0.41$ ) | 40 <sup>a</sup> |
|                       | -0.12                 | -2.09                 | 42 <sup>b</sup> |
|                       | -0.01                 | -1.93                 | 43              |
|                       | -0.21                 |                       | 44 <sup>c</sup> |
|                       | -0.22                 | -1.82                 | 45              |
|                       | -0.06                 |                       | 47              |
|                       | -0.24                 | -2.05                 | 49 <sup>d</sup> |
| Ni (100)              | -0.16                 | -1.61                 | 50              |
|                       | -0.14 ( $q = -0.61$ ) | -2.04 ( $q = -0.52$ ) | 40 <sup>a</sup> |
|                       | -0.25                 | -1.88                 | 43              |
| Ni (110)              | -0.22                 | -1.81                 | 45              |
|                       | -0.42 ( $q = -0.67$ ) | -1.94 ( $q = -0.33$ ) | 40 <sup>a</sup> |
|                       | -0.40                 | -1.87                 | 45              |
| Ni (211)              | -0.47                 |                       | 46              |
|                       | -0.46                 | -1.92                 | 48              |
|                       | -0.93 ( $q = -0.82$ ) |                       | 41              |
|                       | -0.31                 | -2.09                 | 42 <sup>b</sup> |
|                       | -0.38                 | -1.97                 | 43              |
|                       | -0.35                 | -1.82                 | 45              |

<sup>a</sup> Calculated using Cambridge sequential total energy package (CASTEP). <sup>b</sup> Calculated using Spanish Initiative for Electronic Simulations with Thousands of Atoms (SIESTA). <sup>c</sup> Calculated using Material Studio (Dmol<sup>3</sup>). <sup>d</sup> Calculated using Quantum Espresso package (QE).

to CO, *via* hydrogen-assisted  $\text{CO}_2$  dissociation (COOH pathway). However, there exists a high barrier (1.51 eV) rate limiting step, which suggests the high temperature needed (above 810 °C) to achieve the RWGS reaction.

Most reported studies on  $\text{CO}_2$  adsorption on nickel catalysts are based on theoretical methods. Recently, there has been some progress in the *operando* study of  $\text{CO}_2$  adsorption. Yuan *et al.*<sup>58</sup>

observed in *operando* the dissociation of  $\text{CO}_2$  on the Ni (111) surface at temperatures between 300 and 900 K *via* near ambient pressure X-ray photoelectron spectroscopy (NAP-XPS), corroborated by low energy electron diffraction (LEED) and scanning tunneling microscopy (STM) measurements. They found that  $\text{CO}_2$  quickly reacts with the clean nickel. Various Ni-O phases form even at room temperature: initially the  $p(2 \times 2)$ -structured Chem-O (as shown in Fig. 2d), followed by epitaxial NiO (111) with a sodium chloride structure, and finally an oxygen enriched surface layer of  $\text{Ni}_2\text{O}_3$  at the oxidative potential.<sup>58</sup> The accumulation rate of the Ni-O phases under  $\text{CO}_2$  has a negative correlation with temperature. This suggests that the dynamic oxygen concentration is not limited by  $\text{CO}_2$  activation. The thermal decomposition of the Ni-O phases plays an important role. The Ni-O phases exhibit carbon-phobic properties due to repulsive forces to the  $\text{CO}$  adsorbate and lower C-H bond scission rates than metallic Ni. This causes the intrinsic coke resistance.<sup>58</sup> As shown in Fig. 2a–c, the products of the two adsorption modes (dissociative and non-dissociative) can be observed even at 300 K, except that the C 1s peak for  $\text{CO}$  is absent.<sup>58</sup> The reason for the absence of  $\text{CO}$  and the presence of  $\text{CO}_2^{\delta-}$  was explained by the weakened bond between  $\text{CO}$  and the oxidized surface.<sup>58</sup> The content of  $\text{CO}_2^{\delta-}$  decreases with increasing temperature. This suggests its weak bonding to the surface or the dissociative adsorption as the domain mechanism.

## 4. $\text{CO}_2$ hydrogenation to methane

$\text{CO}_2$  methanation is exothermic (reactions (3) and (4) in Table 1). It is thermodynamically favoured. The supported nickel catalyst is active for  $\text{CO}_2$  methanation. Most reported Ni catalysts of  $\text{CO}_2$  hydrogenation were for methane synthesis. However, there exists a kinetic limitation at reasonably low

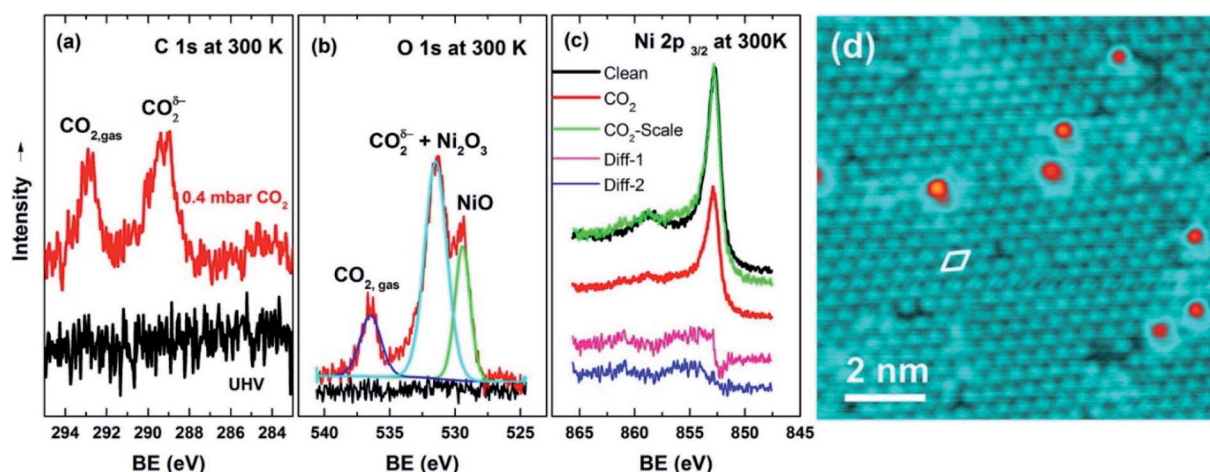


**Fig. 2** (a–c) NAP-XP spectra of C 1s, O 1s, and Ni  $2p_{3/2}$  at 300 K. The spectra in black were measured in a ultra high vacuum (UHV), and those in red were measured under 0.4 mbar  $\text{CO}_2$ . In (c), the green spectrum was obtained from rescaling the red one (0.4 mbar  $\text{CO}_2$ ) to be comparable with the black one (in UHV). The pink spectrum "Diff-1" was the difference spectrum between the green and the black, and the blue spectrum "Diff-2" was the difference spectrum with energy correction (the green shifted by 0.08 eV minus the black). (d) The STM image of a  $p(2 \times 2)$  structure formed on Ni (111) after exposure to 100 L  $\text{CO}_2$  at room temperature. The unit cell is marked by a white diamond and was measured as  $0.51 \pm 0.03$  nm. The bias voltages and tunneling currents were  $-0.2$  V and  $0.1$  nA. The red dots here refer to the undesorbed  $\text{CO}$ .<sup>58</sup> Copyright 2016, American Chemical Society.

temperatures for CO<sub>2</sub> methanation on the supported Ni catalyst. The catalyst structure has a big effect on the activity and selectivity of the supported Ni catalyst for CO<sub>2</sub> methanation. The mechanism for CO<sub>2</sub> methanation on the supported Ni catalyst is still in debate, mostly because of the difficulty in the identification of the catalyst structure. The preparation of a Ni catalyst with a controllable structure remains a big challenge. Significant efforts are being made to reach the goal toward a supported nickel catalyst with a clear mechanism and enhanced low temperature activity for CO<sub>2</sub> methanation.

#### 4.1 Theoretical studies

According to Table 2, the adsorption of CO on the Ni surface is very stable with an adsorption energy around  $-2.0$  eV. Therefore, the reaction barrier for CO<sub>2</sub> dissociation decides whether the reaction takes the CO (derived from direct CO<sub>2</sub> dissociation) pathway or formate (derived from hydrogen-assisted CO<sub>2</sub> dissociation) pathway. The corresponding reactions and their barriers are listed in Table 3.<sup>41,42,46,47,59–64</sup> The strong binding of CO on the Ni catalyst can block the CO<sub>2</sub> adsorption and H<sub>2</sub> dissociation, which decreases the activity of the catalyst. In addition, the strongly bound CO species can be directly and indirectly dissociated to C species, which may result in the deactivation of the catalyst by carbon deposition over Ni particles.<sup>59</sup> The dissociated adsorption of H<sub>2</sub> on Ni surfaces is also important. The stronger dissociated adsorption of H<sub>2</sub> makes the adsorption of H species compete with CO adsorption, which promotes the hydrogenation of CO or C to form methane. The weaker dissociated adsorption of H<sub>2</sub> can facilitate the CO<sub>2</sub> hydrogenation to form COOH\* or HCOO\* species. For example, the reaction barrier for CO<sub>2</sub> dissociation on Ni (211) ( $E_a = 0.82$  eV) is higher than that on Ni (111) ( $E_a = 0.57$  eV) as shown in Table 3.<sup>41,42,46,47,59–64</sup> The stronger dissociated adsorption of H<sub>2</sub> on Ni (111) makes the adsorption of H species compete with CO adsorption, which promotes CO hydrogenation or C hydrogenation to form methane. The weaker dissociated adsorption of H<sub>2</sub> on Ni (211) can facilitate CO<sub>2</sub> hydrogenation to form COOH\* or HCOO\* species.

The hydrogenation of CO is favourable on low-index Ni surfaces, such as Ni (111), because the small barrier for CO<sub>2</sub> dissociation and strong adsorption energy of CO on Ni (111) make CO the dominant species on Ni (111). As predicted by a DFT study, the chemisorption of CO<sub>2</sub> on Ni (111) is not energetically favored.<sup>40</sup> However, CO and atomic oxygen, products of CO<sub>2</sub> dissociation, bind strongly to nickel. The full reaction pathway is shown in Fig. 1. Once the CO species is formed on the surface (as CO\*), hydrogenation of CO to CHO\* ( $E_a = 1.35$  eV (ref. 42)) is more favourable than COH\* ( $E_a = 1.81$  eV (ref. 42)). Even COH\*, formed on Ni (111), prefers to be dissociated to CO\* because of the low backward reaction barrier ( $E_a = 0.85$  eV (ref. 42)). Further dissociation of CHO\* to CH\* has a 1.28 eV barrier and the subsequent addition of H to CH\* to form CH<sub>4</sub> with small barriers<sup>65</sup> (Ni (111): CH\* + H\* → CH<sub>2</sub>\*,  $E_a = 0.52$  eV (ref. 62) and CH<sub>2</sub>\* + 2H\* → CH<sub>4</sub>(g),  $E_a = 0.50$  eV (ref. 62)). Since CO<sub>2</sub> methanation is an exothermic reaction, the heat accumulation from the reaction promotes the dissociation of

**Table 3** Reaction barriers (in eV) for important elementary reactions involved in the CO<sub>2</sub> methanation. The data outside and inside the parentheses represent the forward and backward reaction barriers (unit: eV)

| Surface  | CO <sub>2</sub> * → CO* + O* | H* | CHO* → CO* + H*                                      | CO* + H* → CH* + O*      | COH* + H* → CO* + H <sub>2</sub> O | COOH* + H* → CO* + H <sub>2</sub> O | CO* + H* → COOH* + O*    | HCOO* + H* → CO* + H <sub>2</sub> O | HCOO* + H* → CO* + H <sub>2</sub> O | CO* + H* → C* + O* | Ref.   |
|----------|------------------------------|----|--|--------------------------|------------------------------------|-------------------------------------|--------------------------|-------------------------------------|-------------------------------------|--------------------|--|
|          |                              |    |  |                          |                                    |                                     |                          |                                     |                                     |                    |  |
| Ni (111) | 0.57(1.53)<br>0.78(1.32)     |    | 0.20(1.35)<br>0.32(1.64)<br>0.18(1.51)<br>0.31(1.59) | 1.28(1.43)<br>1.28(0.89) |                                    |                                     |                          |                                     |                                     |                    | 42 <sup>a</sup><br>59 <sup>b</sup><br>60 <sup>c</sup><br>61 <sup>d</sup> |
| Ni (100) | 0.53                         |    | 0.79(1.36)   |                          |                                    |                                     |                          |                                     |                                     |                    | 47   |
| Ni (110) |                              |    |  |                          |                                    |                                     |                          |                                     |                                     |                    | 62 <sup>e</sup><br>63  |
| Ni (211) | 0.82(1.57)<br>0.46(0.92)     |    | 0.37(1.46)   | 0.86(1.16)               |                                    |                                     |                          |                                     |                                     |                    | 60 <sup>c</sup><br>46  |
|          |                              |    |  |                          | 0.24(1.17)                         |                                     |                          |                                     |                                     |                    | 64 <sup>f</sup>  |
|          |                              |    |  |                          |                                    | 0.34(0.27)                          |                          |                                     |                                     |                    | 42 <sup>a</sup><br>41  |
|          |                              |    |  |                          |                                    |                                     | 0.70(0.28)<br>0.71(0.62) |                                     |                                     |                    |  |
|          |                              |    |  |                          |                                    |                                     |                          | 1.49(0.59)<br>1.08(0.99)            |                                     |                    |  |
|          |                              |    |  |                          |                                    |                                     |                          |                                     | 2.97                                |                    |  |
|          |                              |    |  |                          |                                    |                                     |                          |                                     |                                     | 3.01(1.59)         |  |

<sup>a</sup> Calculated using SIESTA. <sup>b</sup> Calculated using Cambridge sequential total energy package (CASTEP). <sup>c</sup> Calculated using Simulation Tool for Atom Technology (STATE). <sup>d</sup> Calculated using DACAPO package. <sup>e</sup> Calculated based on atom superposition and electron delocalization molecular orbital (ASED-MO) theory. <sup>f</sup> Calculated using QUANTUM ESPRESSO Package (QE).

CO ( $E_a = 3.01$  eV (ref. 42)) or other intermediates, such as COH\* ( $E_a = 2.07$  eV (ref. 42)), CHO\* ( $E_a = 1.28$  eV (ref. 42)) and CH\* ( $E_a = 1.32$  eV (ref. 42)) to carbon species.

However, it is favourable for CO<sub>2</sub> methanation over Ni (211) or Ni (110) to proceed through direct CO<sub>2</sub> hydrogenation because of the lower barrier for CO<sub>2</sub> hydrogenation to HCOO\* ( $E_a = 0.70$  eV (ref. 42 and 64)) than CO<sub>2</sub> dissociation ( $E_a = 0.82$  eV (ref. 42)) and weaker H binding energies than on Ni (111). CO<sub>2</sub> hydrogenation to form COOH\* with a barrier around 0.70 eV (ref. 42 and 64) is followed by the hydrogenation of COOH\* to COHOH\* ( $E_a = 0.34$  eV (ref. 64)). Further dissociation of COHOH\* to HCOH\* has a 0.24 eV barrier.<sup>64</sup> Hydrogenation of HCOH\* to CH<sub>2</sub>OH\* has a barrier of 1.00 eV (ref. 64) and further hydrogenation to CH<sub>3</sub>\* has a barrier of 1.47 eV.<sup>64</sup> The reaction pathway through HCOO\* to form CH<sub>4</sub> presented in Fig. 1 is less favourable than through COOH\* due to the higher barrier required for the hydrogenation of methoxy (CH<sub>3</sub>O\*) to CH<sub>4</sub>.

On the other hand, HCOO\* is considered as the key intermediate for producing methanol, especially on In<sub>2</sub>O<sub>3</sub> and Cu-based catalysts.<sup>66–71</sup> Studies by Schatz and his co-workers<sup>72</sup> suggested that the formation of HOCO\*, HCOO\*, HCO<sub>3</sub>\* and CO\* on Ni (110) is theoretically feasible during CO<sub>2</sub> hydrogenation. The reaction temperature, CO<sub>2</sub> coverage on the surface and the energy of the hydrogen atom determine which intermediates would be formed and which product would be obtained.<sup>72</sup>

The support has a significant effect on CO<sub>2</sub> methanation over the supported nickel catalyst.<sup>8–20,73,74</sup> It has a big influence on the adsorption of the reactants, desorption, electron density of the supported Ni catalyst and Ni-support interactions. Among various supporting materials, CeO<sub>2</sub> has been extensively investigated.<sup>10,15,73–78</sup> CeO<sub>2</sub> shows a better activity and a close to 100% selectivity toward CH<sub>4</sub> than other supporting materials.<sup>77,78</sup> The perfect CeO<sub>2</sub> surface shows poor ability for CO<sub>2</sub> or CO chemisorption or activation. The adsorption energies of CO<sub>2</sub> and CO on CeO<sub>2</sub>(111) are  $-0.27$  (ref. 55) and  $< -0.2$  eV, respectively.<sup>79,80</sup> CeO<sub>2</sub> stabilizes the Ni particle and increases its activity by elongating the bond length of Ni–Ni when Ni is loaded on the CeO<sub>2</sub> surface. CeO<sub>2</sub> enhances the activation of CO<sub>2</sub> at the interface of Ni particles and the CeO<sub>2</sub> surface and promotes the adsorbed CO<sub>2</sub> species to react with the H atoms on nickel to produce methane through the COOH reaction pathway.

The strong reducibility of CeO<sub>2</sub> facilitates the creation of O vacancies. CeO<sub>2</sub>(110) and (111) surfaces with O vacancies favour CO oxidation but further oxidation of CO<sub>2</sub> to carbonate is kinetically hindered due to too much electron accumulation on O vacancies.<sup>81</sup> In addition, loading Ni clusters on the CeO<sub>2</sub> surface was found to be favourable for the oxidization of C to CO and for further CO oxidation. CeO<sub>2</sub> thus improves the resistance of carbon deposition from CO decomposition by facilitating the oxidization of C and CO. This leads to enhanced coke resistance for CO<sub>2</sub> methanation.

## 4.2 Operando studies based on the single crystal

To study the mechanism of CO<sub>2</sub> methanation over a supported Ni catalyst, an *operando* study is also important. By means of infrared-visible sum frequency generation (IR-vis SFG) vibrational spectroscopy and NAP-XPS, Roiaz *et al.*<sup>82</sup> studied the hydrogenation of CO and CO<sub>2</sub> on the Ni (110) single crystal at  $10^{-1}$  mbar *in situ* as a function of the surface temperature in the range of 300–525 K. In addition to atomic carbon and precursors for graphenic carbon phases, five non-equivalent CO species have been distinguished, which confirms co-adsorption of H and C atoms, H-induced activation of CO, and surface reconstruction. At low temperatures, carbonate species are produced by the interaction of CO<sub>2</sub> with atomic oxygen, which stems from the dissociation of \*CO<sub>2</sub> into \*CO + \*O. A metastable activated CO<sub>2</sub><sup>–</sup> species is also detected. This species can be at the same time a precursor state toward dissociation into CO and O in the RWGS mechanism and a reactive species that undergoes direct hydrogenation conversion in the CO<sub>2</sub> methanation process.<sup>82</sup> This suggests that CO<sub>2</sub> methanation occurs through the two parallel routes.

Using AP-XPS, Heine *et al.*<sup>83</sup> investigated the adsorption and reactions of CO<sub>2</sub> and CO<sub>2</sub> + H<sub>2</sub> on the Ni (111) surface to identify the surface chemical state and the nature of the adsorbed species during the methanation reaction. In 200 mTorr CO<sub>2</sub>, they found that NiO is formed from CO<sub>2</sub> dissociation into CO and atomic oxygen. Moreover, carbonate (CO<sub>3</sub><sup>2–</sup>) is present on the surface from further reaction of CO<sub>2</sub> with NiO, as shown in Fig. 3. The addition of H<sub>2</sub> into the reaction environment leads to the reduction of NiO and the disappearance of CO<sub>3</sub><sup>2–</sup>. They found that CO adsorbed on hollow sites, atomic carbon and OH species are present on the surface at temperatures  $> 160$  °C. Their study suggested that the methanation reaction proceeds *via* direct dissociation of CO<sub>2</sub>. The reduction of CO is then followed to atomic carbon. The further hydrogenation of atomic carbon leads to the formation of methane. However, carbon formation on a nickel catalyst is an important but complex issue. The carbon formation of supported Ni catalysts may cause deactivation during CO<sub>2</sub> methanation. Previous studies have confirmed that the Ni (111) facet possesses the correct symmetry and low lattice mismatch for graphene growth.<sup>84–86</sup> This would explain the better reactivity of the catalyst with more Ni (111) for CO<sub>2</sub> methanation<sup>87,88</sup> since graphene like carbon tends to form methane during the hydrogenation. Hu *et al.*<sup>89</sup> also found that coke is unlikely to form on Ni (111) during CO<sub>2</sub> reforming of methane. The carbon species formed on Ni (111) have better reactivity with hydrogen and CO<sub>2</sub>.<sup>90</sup> Patera *et al.*<sup>91</sup> reported an atomic-scale description of the structure of graphene edges on Ni (111), both during and post growth, by using STM. They demonstrated that temperature acts as a control parameter driving the structure of graphene/Ni (111) edges by changing their passivation. When graphene forms above a Ni (111) substrate (*i.e.*, at  $T > 300$  °C), during the growth process, its edges are clean and anchored to the metal substrate. This confirms the theoretical prediction by Zhang *et al.*<sup>92</sup> Growing graphene flakes are thus sealed, most probably thereby hindering the penetration of ad-species below the flakes. Upon cooling to room



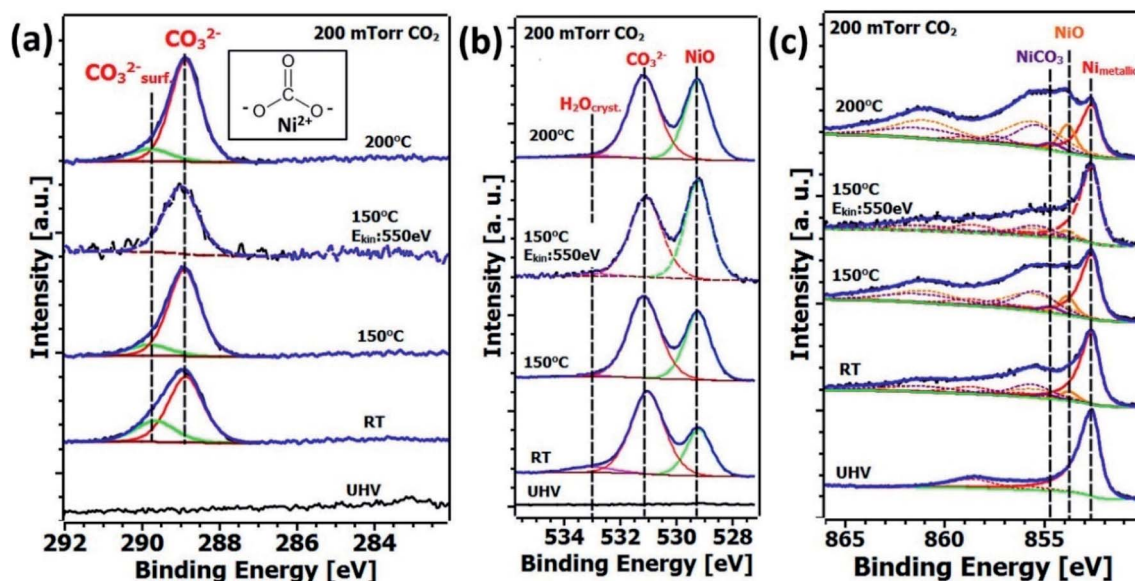


Fig. 3 Oxidation of Ni (111) in a CO<sub>2</sub> atmosphere. (a) C 1s, (b) O 1s, and (c) Ni 2p<sub>3/2</sub> in 200 mTorr CO<sub>2</sub> in the temperature range from room temperature to 200 °C. All spectra are recorded at a kinetic energy of 200 eV, except where labels indicate a more bulk-sensitive measurement at  $E_{\text{kin}} = 550$  eV. Inset: molecular structure of NiCO<sub>3</sub>.<sup>83</sup> Copyright 2016, American Chemical Society.

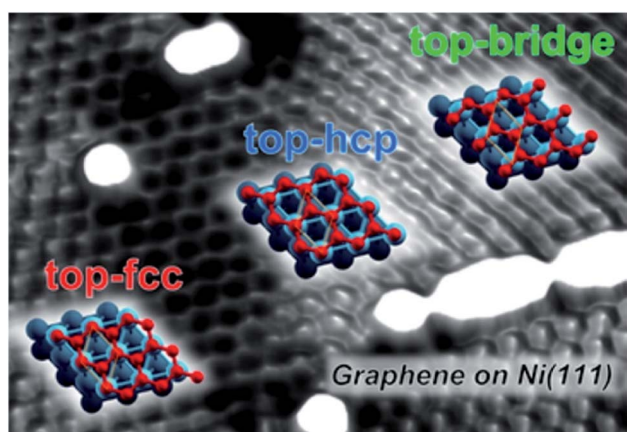


Fig. 4 The atomic description of graphene on Ni (111).<sup>93</sup> Copyright 2014, American Chemical Society.

temperature, the growth is stopped, and supported graphene flakes are formed. Fig. 4 shows an illustrated STM image of graphene on Ni (111).<sup>93</sup> Patera *et al.*<sup>94</sup> recently reported real-time imaging of adatom promoted graphene growth on Ni (111) by means of *in situ* high speed STM measurements. By monitoring layer formation at the atomic scale and with a time resolution down to milliseconds, at the kink sites of the graphene edges, it was observed that single Ni atoms are involved directly in the graphene growth process. Based on the DFT study, it can be observed that reaction barriers are substantially lower for the carbon (C) atom addition driven by Ni adatoms.

Methods used for graphene studies can be easily extended to the investigation of CO<sub>2</sub> methanation on not just Ni (111). A Ni (111) substrate could enhance the reactivity of the carbon formed because of charge hybridization. In addition, the

surface reactivity of the nickel catalyst can be strongly modulated by surface carbon structures.<sup>95</sup> The content or the thickness of the formed carbon also has a significant effect for further reactions.<sup>84</sup>

#### 4.3 Operando studies of the nickel catalysts on the porous supports

The *operando* studies and/or the *in situ* characterization of supported nickel catalysts for CO<sub>2</sub> hydrogenation is obviously more complex and more challenging. For the investigation of the structural effect of nickel catalysts on CO<sub>2</sub> methanation, studies based on single crystals may not be suitable because they lack the influence of electronic effects.<sup>96</sup> Increasing publications can be found in the literature on the *operando* studies and/or the *in situ* characterization of nickel catalysts supported by a porous support, in order to understand the dynamic evolution of the catalyst structure during the reaction, to investigate the nickel-support interaction, and to ensure the optimum condition for catalyst preparation.

Using *operando* X-ray absorption spectroscopy (XAS) analyses, Mutz *et al.*<sup>97</sup> found that a fast bulk-like oxidation of the Ni particles occurred immediately after the removal of hydrogen from the gas stream, during their study on CO<sub>2</sub> methanation over a Ni/CaO–Al<sub>2</sub>O<sub>3</sub> catalyst with high Ni loading (23 wt%) at a H<sub>2</sub>/CO<sub>2</sub> feed ratio of 4/1. In the following methanation step, a lower catalytic performance was observed due to residuals of partly oxidized Ni. This indicates that an efficient reactivation step is necessary after a H<sub>2</sub> dropout to return to the initial activity. These results are important for CO<sub>2</sub> methanation applications operating under more realistic conditions, where the fluctuating supply of hydrogen has to be considered. Consequently, oxidation of the catalyst has to be prevented or efficient reactivation procedures need to be developed.<sup>97</sup>



Table 4 Reaction intermediates on the supported nickel catalysts in CO<sub>2</sub> methanation

| Wavenumber (cm <sup>-1</sup> ) |  |                             |                               |                    |                            |                               |                             |                                   |  |                             |   |  |  |
|--------------------------------|--|-----------------------------|-------------------------------|--------------------|----------------------------|-------------------------------|-----------------------------|-----------------------------------|--|-----------------------------|---|--|--|
| Species                        | Type or vibration mode   | TiO <sub>2</sub> (ref. 100) | NaY <sup>101</sup> (ref. 101) | NaZSM-5 (ref. 101) | SiO <sub>2</sub> (ref. 96) | MgO <sup>3,5</sup> (ref. 102) | ZrO <sub>2</sub> (ref. 102) | Cubic ZrO <sub>2</sub> (ref. 108) | Y <sub>2</sub> O <sub>3</sub> (ref. 104) | CeO <sub>2</sub> (ref. 103) | CeO <sub>2</sub> nanoplates <sup>105</sup> (ref. 106) | Mesoporous CeO <sub>2</sub> (ref. 109) | CeO <sub>2</sub> (ref. Platelet SBA-15 (ref. 107)) |
| CH <sub>4</sub> gas            | δ(CH)<br>ν(CH)   |                             |                               |                    |                            | 1305<br>3016                  | 1305<br>3015                |                                   |  |                             | 1300<br>3000  | 1306<br>3014<br>2065                   | 1300<br>3000<br>2066                               |
| Subcarbonyl                    | Ni(CO) <sub>n</sub> (n = 2 or 3)   |                             |                               |                    |                            |                               |                             |                                   |  |                             |   |  |  |
| Linear CO*                     | ν(CO)  |                             |                               |                    | 2060                       |                               | 2100–1950                   | 2028                              |  | 2027                        | 2040  | 2050–2020                              | 2050<br>2035                                       |
| Bridged CO*                    | ν(CO)  | 1817                        |                               |                    | 1903                       |                               | 1950–1750                   | 1923, 1867                        |  | 1923, 1852                  | 1920  | 1930–1920                              | 1912   |
| Multibonded CO*                | ν(CO)  |                             |                               |                    |                            |                               |                             |                                   |  |                             |   | 1860–1840                              |  |
| Bidentate carbonate            | ν <sub>as</sub> (CO <sub>3</sub> )<br>ν <sub>as</sub> (CO <sub>3</sub> )<br>ν <sub>s</sub> (CO <sub>3</sub> )<br>ν <sub>s</sub> (CO <sub>3</sub> )<br>ν <sub>as</sub> (CO <sub>3</sub> ) | 1540<br>1523<br>1479        | 1681                          |                    |                            |                               | 1552<br>1537<br>1320        | 1640<br>1486<br>1402<br>1296      | 1602<br>1559                             |                             | 1564  | 1580                                   | 1285   |
| Bicarbonate                    |  | 1618, 1670                  | 1627                          | 1643               |                            | 1650                          | 1625                        | 1630                              |  |                             | 1634  |  |  |
|                                | ν <sub>s</sub> (CO <sub>3</sub> )  | 1442                        | 1430                          | 1440               |                            |                               | 1416                        | 1367                              | 1438                                     |                             | 1432  |  |  |
|                                | δ(OH)  | 1489                        |                               |                    |                            | 1250                          | 1220                        | 1218                              |  |                             |   |  |  |
| Bidentate formate              | ν <sub>as</sub> (CO <sub>2</sub> )   | 1589                        | 1546                          |                    | 1591                       | 1606–1596                     | 1572                        | 1578                              | 1560–1588                                | 1580                        |   | 1550                                   | 1647   |
|                                | ν <sub>s</sub> (CO <sub>2</sub> )  | 1378                        |                               |                    |                            | 1343                          | 1356                        | 1350                              |  | 1365                        | 1370<br>2850  | 1360<br>2945, 2845                     | 1437   |
|                                | ν(CH)  |                             |                               |                    |                            |                               | 2867                        |                                   |  |                             |   |  |  |
| Monodentate formate            | δ(CH)<br>ν <sub>as</sub> (CO <sub>2</sub> )<br>ν <sub>s</sub> (CO <sub>2</sub> )   | 1404                        |                               |                    |                            | 1386                          | 1386                        |                                   |  | 1387                        |   | 1610<br>1333                           |  |
|                                |  |                             |                               |                    |                            |                               | 1610<br>1332                |                                   | 1338–1348                                |                             |   |  |  |
| Monodentate carbonate          | ν <sub>as</sub> (CO <sub>3</sub> )<br>ν <sub>as</sub> (CO <sub>3</sub> )<br>ν <sub>s</sub> (CO <sub>3</sub> )  |                             |                               |                    |                            | 1529<br>1435                  | 1521<br>1450<br>1335        | 1518                              |  | 1520<br>1480<br>1287        |   | 1530                                   | 1390   |
| Methylene                      | ν(CH)  | 2873                        |                               |                    |                            |                               |                             |                                   |  |                             |   |  |  |
| Methyl                         | ν(CH)  | 2935                        |                               |                    |                            |                               |                             |                                   |  |                             |   | 1475                                   |  |
| Methoxy                        | ν(CO)  | 1735                        |                               |                    |                            |                               |                             | 1436                              | 1328                                     | 1287                        |   | 1395                                   |  |
| Formyl                         | ν(CO)  |                             | 1357                          | 1346               |                            |                               |                             |                                   |  |                             |   |  | 1750   |

Vogt *et al.*<sup>96</sup> applied quick *operando* XAS, together with *operando* transmission Fourier transform infrared (FT-IR) analyses, to study the size effect and thus the structure sensitivity of the SiO<sub>2</sub> supported Ni catalysts for CO<sub>2</sub> hydrogenation. By this study, they found that the sub-2 nm Ni particle possesses a lower d-band energy or higher electron localization, compared to large nanoparticles. This has a considerable impact on the catalytic activity.<sup>96</sup> The Ni particles with a smaller size tend to produce CO, while the catalysts with a larger size tend to favour methane formation,<sup>96,98,99</sup> although the formation of methane was observed for the smallest Ni clusters (~1 nm).<sup>96</sup> If the supported nickel catalyst further goes down to single atoms, only carbon monoxide is produced from CO<sub>2</sub> hydrogenation.<sup>35</sup> Moreover, the product formation rate increases by a factor of 3 at the same temperature after the particle is formed.<sup>35</sup> The origin of the structure sensitivity of Ni/SiO<sub>2</sub> for CO<sub>2</sub> hydrogenation was considered to be the electronic structure of the nickel catalyst within the nickel size of 1–7 nm.<sup>96</sup> However, if the catalyst size increases to 8–21 nm, the size effect is not the consequence of electronic effects scaling with size.<sup>99</sup> It would be caused by the increase in the relative abundance of the active sites resulting from the change of the geometric structure.<sup>99</sup>

The *operando* diffuse reflectance infrared Fourier transform (DRIFT) study is very useful for the study of the structural effect of supported nickel catalysts on the adsorption, surface reaction, conversion pathway and desorption for CO<sub>2</sub> hydrogenation to methane.<sup>35,96,99–109</sup> With the *in situ* DRIFT or the *operando* transmission FT-IR analyses, CO<sub>2</sub> adsorption (and related CO adsorption) on the supported nickel catalyst has been well investigated. Some of the key intermediates, as presented in Fig. 1, can be identified. Table 4 presents some illustrative identified infrared vibrational bands and the assigned types on the supported nickel catalyst during CO<sub>2</sub> methanation.<sup>35,96,99–109</sup> The reactive pathway(s) can be thus identified. If the catalyst takes the direct CO<sub>2</sub> dissociative pathway, carbonyls (CO\*) can be identified, followed by CO hydrogenation to form methane.<sup>106</sup> If the catalyst takes the hydrogen-assisted CO<sub>2</sub> dissociation pathway, oxygenate intermediates can be observed.<sup>106</sup>

Jia *et al.*<sup>102</sup> reported an *operando* DRIFT study of the structural effect of Ni/ZrO<sub>2</sub> with Ni (111) as the principal exposed facet on CO<sub>2</sub> methanation. The CO<sub>2</sub> adsorption was firstly investigated in the temperature range of 50–350 °C. At 50 °C, bands at 1625, 1416 and 1220 cm<sup>-1</sup> are observed. These bands are attributed to bidentate bicarbonate species. A band at 1335 cm<sup>-1</sup>, assigned to monodentate carbonates, is also observed. With the increasing temperature, the band intensities for the bicarbonates reduce monotonically. However, new bands for bidentate formates (1572 and 1356 cm<sup>-1</sup>), bidentate carbonates (1552, 1537 and 1320 cm<sup>-1</sup>) and monodentate carbonates (1521, 1450 and 1335 cm<sup>-1</sup>) present with gradually increased intensities. Meanwhile, monodentate carbonates increase more rapidly than bidentate carbonates above 200 °C. This suggests the good thermal stability of monodentate carbonates. The DRIFT studies verify that OH groups on the ZrO<sub>2</sub> surface provide weakly basic sites for bicarbonates, whereas acid–base Zr<sup>4+</sup>–O<sup>2-</sup> pairs and O<sup>2-</sup> sites serve as

moderately and strongly basic sites for bidentate and monodentate carbonates.<sup>102</sup> The bands related to adsorbed CO (CO\*) in linear and bridge forms on the Ni surface are visible in 2100–1950 cm<sup>-1</sup> and 1950–1750 cm<sup>-1</sup>. The adsorbed CO should be formed from direct CO<sub>2</sub> dissociation (CO<sub>2</sub>\* → CO\* + O\*) on the Ni (111) facets, followed by the reaction with OH groups towards a small amount of formates (CO\* + OH\* → HCOO\*). The appearance of the bands for bidentate formates is good evidence for CO<sub>2</sub> dissociation. The Ni (111) surface facilitates the dissociation of CO<sub>2</sub> into adsorbed CO as a crucial intermediate for methane synthesis.<sup>62,83,110</sup>

*Operando* DRIFT measurements for CO<sub>2</sub> methanation over Ni/ZrO<sub>2</sub> were then conducted.<sup>102</sup> As shown in Fig. 5, at 150 °C, bicarbonates (1625, 1416 and 1220 cm<sup>-1</sup>), monodentate carbonates (1521, 1450 and 1335 cm<sup>-1</sup>) and bidentate formates (2867, 1572, 1384 and 1356 cm<sup>-1</sup>) were observed. Bidentate formates keep substantially increasing up to 200 °C, accompanied by a decrease of both bidentate bicarbonates and monodentate carbonates. However, bidentate carbonates are invisible due to their instability and rapid decomposition before hydrogenation to formates. The appearance of a shoulder band at 1610 cm<sup>-1</sup>, which is typically attributed to monodentate formates, is worth noting. It has been proposed that bidentate formates originate from hydrogenation of bidentate bicarbonates, and monodentate formates are derived from the hydrogenation of monodentate carbonates. A smaller amount of monodentate formates left on the catalyst is mainly due to their faster hydrogenation and decomposition. It is sure that Ni/ZrO<sub>2</sub> with Ni (111) as the principal exposed facet significantly improves the activity of the (bi)carbonate hydrogenation towards bidentate and monodentate formates.<sup>102</sup>

*Operando* DRIFT analyses were further conducted to study the evolution of adsorbed and gaseous species as a function of

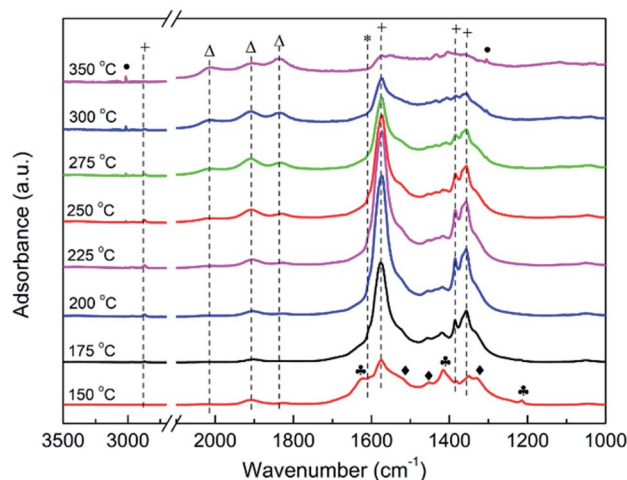


Fig. 5 *Operando* DRIFT spectra during the temperature-programmed reaction of a gas mixture (40 mL min<sup>-1</sup>) containing 2.5% H<sub>2</sub>, 0.5% CO<sub>2</sub> with argon as a carrier gas over Ni/ZrO<sub>2</sub>. The heating rate is 10 °C min<sup>-1</sup>. Symbol definition: bidentate bicarbonate (♣), monodentate carbonate (◆), bidentate formate (+), monodentate formate (\*), linear CO or bridge CO (Δ) and gaseous CH<sub>4</sub> (●).<sup>102</sup> Copyright 2018, Elsevier.

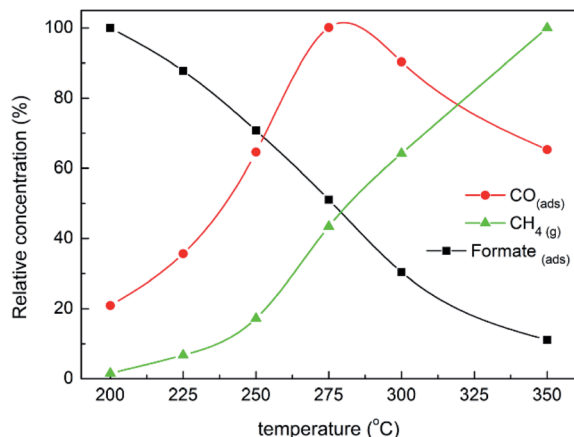


Fig. 6 Variation of relative concentrations of  $\text{CH}_4(\text{g})$  ( $3015\text{ cm}^{-1}$ ), adsorbed CO ( $2100\text{--}1750\text{ cm}^{-1}$ ) and bidentate formates ( $1572\text{ cm}^{-1}$ ) during temperature-programmed  $\text{CO}_2$  methanation over  $\text{Ni/ZrO}_2$ .<sup>102</sup> Copyright 2018, Elsevier.

the temperature<sup>102</sup> with the calculated relative concentrations of bidentate formates and adsorbed CO as well as gaseous methane. The quantification of adsorbed CO was made by the integration of bands in the range of  $2100\text{--}1750\text{ cm}^{-1}$ , while the quantifications of formates and methane were made following the band intensities at  $1572$  and  $3015\text{ cm}^{-1}$ . The highest value measured for every species was set to 100.0% in order to obtain normalized relative concentrations from 200 to 350 °C. As shown in Fig. 6, with increasing temperature from 200 to 250 °C, a gradual decrease of formates is induced from 100.0% to 70.1%, accompanied by the respective increase of adsorbed CO and methane from 20.9 to 64.6% and 1.6 to 17.2%. These confirm that the dissociation of formates into adsorbed CO is dominant for formate conversion at first.<sup>102</sup> Above 250 °C, the methane production rate is significantly boosted by the hydrogenation steps. The adsorbed CO reaches the maximum at 275 °C, and then begins to be consumed to form methane. Considering the respective evolution of adsorbed CO and methane with the temperature, it is reasonable that methane production is mainly limited by the rate-limiting steps of CO

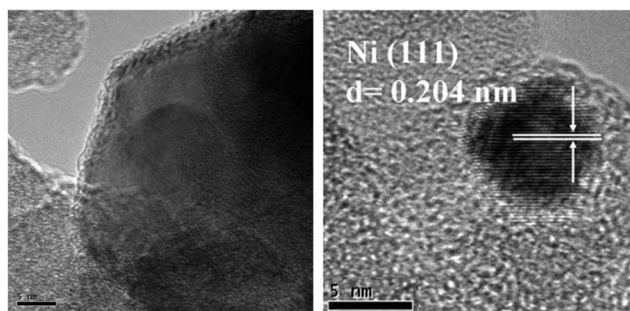


Fig. 7 High-resolution TEM images of the Ni particles in (left)  $\text{Ni/SiO}_2$  prepared *via* decomposition of the nickel precursor thermally; and (right)  $\text{Ni/SiO}_2$  *via* decomposition of the nickel precursor by energetic species of cold plasma. Both samples were reduced by flowing hydrogen at 500 °C for 2 h.<sup>111</sup> Copyright 2013, Elsevier.

dissociation and hydrogenation. In addition,  $\text{CO}_2$  methanation over  $\text{Ni/ZrO}_2$  with Ni (111) as the principal exposing facet prefers to proceed *via* the direct hydrogenation of formates ( $\text{formate}^* \rightarrow \text{CH}_4(\text{g})$ ) and the formate dissociation followed by the hydrogenation of adsorbed CO ( $\text{formate}^* \rightarrow \text{CO}^* \rightarrow \text{CH}_4(\text{g})$ ).

#### 4.4 Structural studies *via* the size effect

$\text{CO}_2$  hydrogenation to methane over a supported nickel catalyst is structure sensitive. It is very important to prepare Ni catalysts

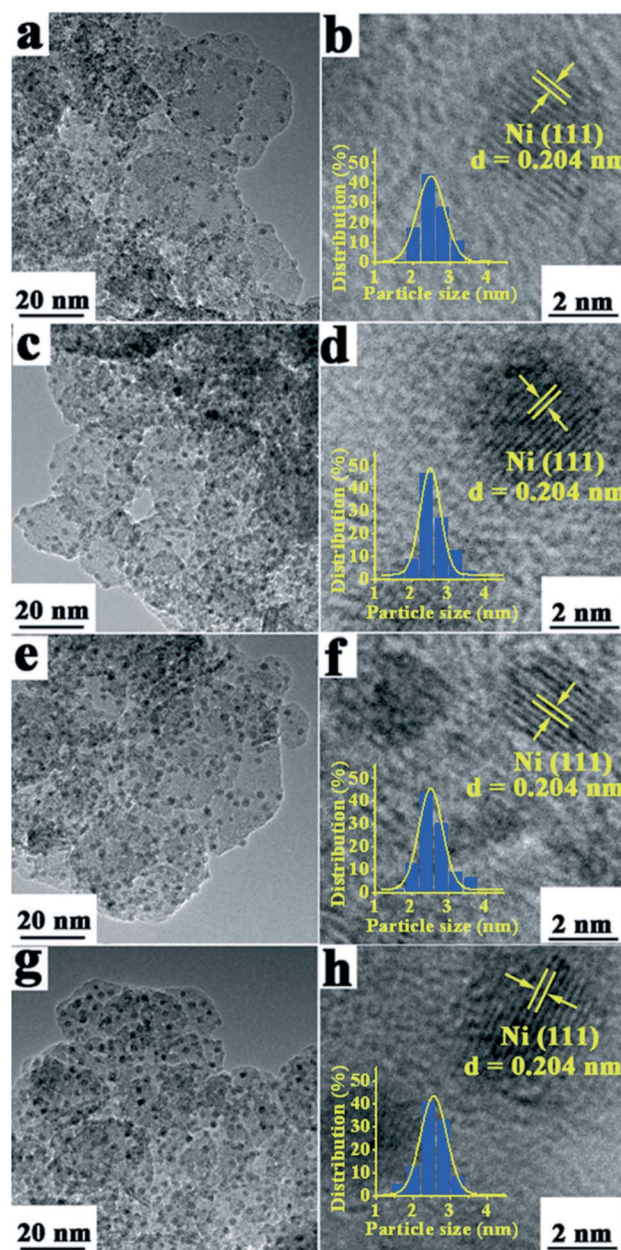


Fig. 8 High resolution transmission electron microscope (HRTEM) images of the  $\text{Ni}_x/\text{Mg}_{2-x}\text{Al-MMO}$  samples: (a and b)  $\text{Ni}_{0.4}/\text{Mg}_{1.6}\text{Al-MMO}$ , (c and d)  $\text{Ni}_{0.8}/\text{Mg}_{1.2}\text{Al-MMO}$ , (e and f)  $\text{Ni}/\text{MgAl-MMO}$  and (g and h)  $\text{Ni}_{1.6}/\text{Mg}_{0.4}\text{Al-MMO}$ . The insets in (b), (d), (f) and (h) show the corresponding particle-size frequency distribution histogram (400 particles analyzed).<sup>117</sup> Copyright 2016, Royal Society of Chemistry.



with a controllable structure. However, obtaining a supported Ni catalyst with a desired structure remains a significant challenge. Only a few studies can be found in the literature on the preparation of catalysts with Ni (111) as the principal exposed face using specific preparation methodologies, such as cold plasma,<sup>87,88,102,111–114</sup> external magnetic field assisted reduction<sup>115</sup> and electrospinning,<sup>116</sup> or using specific supports.<sup>117,118</sup> Fig. 7 and 8 show illustrative images of the supported Ni catalysts with Ni (111) as the principal exposed face.<sup>111,117</sup>

The studies of the structural effect of supported nickel catalysts for CO<sub>2</sub> hydrogenation to methane are mostly *via* the size effect. This means that most of the reported studies affect the catalyst structure *via* the limited nickel nanoparticle size in empirical ways. A decrease in the size of the nickel catalyst causes an increase in the proportion of surface species, surface defects and heterogeneity of the atomic structure. This leads to improved hydrogen activation and enhanced Ni-support interactions. The decreasing particle size enhances the quantum size effects with changes in the electronic nature.<sup>119</sup> A smaller size of the nickel catalysts results in enhanced activity for CO<sub>2</sub> methanation. If the catalyst size goes down to a single nickel atom, the activity of the catalyst may undergo a total change because of the change in the electronic structure, induced by the quantum size effect.

The size effect is highly coupled with the support effect.<sup>120</sup> One can even tune the product of CO<sub>2</sub> hydrogenation from CO to methane with the change of supporting materials for the nickel catalysts of 1 to *ca.* 5 nm.<sup>121</sup>

The inert SiO<sub>2</sub> is an excellent supporting material for the studies of the size effect. Vogt *et al.*<sup>96</sup> applied *operando* transmission FT-IR spectroscopy for their study of the size effect of SiO<sub>2</sub> supported Ni catalysts (within the nickel size of 1–7 nm) for CO<sub>2</sub> hydrogenation. They observed that the catalyst with the highest nickel dispersion or the smallest nickel particle size exhibits relatively few bands assigned to adspecies containing CO stretching vibrations, while the catalyst with the largest size presents big peaks in this region.<sup>96</sup> They found that the intensity of the absorption bands in the CO\* stretching region during CO<sub>2</sub> hydrogenation is positively correlated with the catalyst size.<sup>96</sup> They suggest that this absorption intensity can be an indirect measure for the mean catalyst size.<sup>96</sup> Gaseous CO is detected only for the smaller nickel particles (less than 1.5 nm). The amount of gaseous carbon monoxide is more or less negatively correlated with the catalyst size.<sup>96</sup> All the CO species on the catalyst of small size are easily flushed off, while CO\* presents in much more stable configurations, like bridged carbonyl or carboxylate species, on the catalyst with a larger particle size.<sup>96</sup> Moreover, Vogt *et al.*<sup>96</sup> further used isotopically labelled gas feedstocks (<sup>13</sup>CO<sub>2</sub> and D<sub>2</sub>) for *operando* FT-IR measurements, to investigate the reactivity of the intermediates, such as formate and CO species. Their studies showed that no interaction occurs between the adsorbed <sup>12</sup>C and H in the formate species and the isotopically labelled feedstocks for the catalysts of small Ni particle sizes.<sup>96</sup> For the Ni catalysts of larger particle sizes, however, these labelled gases readily interact and shift the formate peak with both D<sub>2</sub> and <sup>13</sup>CO<sub>2</sub> pulses. They found that the intermediate CO\* species dominate the surface

of the catalysts with larger Ni nanoparticles, while, in the case of catalysts of smaller sizes, formate species dominate the surface with detectable gaseous CO.<sup>96</sup>

Wang *et al.*<sup>120</sup> carried out an *operando* DRIFT study of Ni/SiO<sub>2</sub> for CO<sub>2</sub> methanation with the nickel catalyst size of 3.5–7.5 nm. The activity for CO<sub>2</sub> methanation quickly decreases with increasing catalyst size.<sup>120</sup> The smaller catalysts possess higher reactivity towards CO<sub>2</sub> methanation, whereas the larger catalysts favour the formation of CO, the major by-product. The DRIFT studies indicate that the small nickel catalysts with highly co-ordinately unsaturated surface Ni sites are active for CO<sub>2</sub> methanation through facile adsorption and stabilization of the monodentate carbonate in the adsorption state. This facilitates the formation of monodentate formate species as well as linearly adsorbed CO species, leading to subsequent hydrogenation toward methane.<sup>120</sup>

According to the literature, the following approaches have been mostly employed to limit the size of Ni catalysts: (1) the use of promoter(s); (2) the formation of alloyed catalysts and bi-metallic catalysts; (3) modification of the surface properties of the catalyst or the supporting material; (4) the use of a supporting material with a high surface area; (5) the use of structured catalysts; (6) the use of process intensified preparation methods, such as combustion, cold plasma decomposition of the catalyst precursor, and gel or urea assisted preparation; (7) the application of specific catalyst precursors and others.

Li *et al.*<sup>122</sup> developed a precise control of the growth and size of Ni nanoparticles on Al<sub>2</sub>O<sub>3</sub> by loading of Ni<sup>2+</sup> ions into metal-organic framework (MOF) MIL-110 (Al) *via* incipient wetness impregnation, followed by drying at 120 °C, as well as calcination at 600 °C in air and then hydrogen reduction at 600 or 800 °C. An up to ~20 wt% Ni loading was applied. The particle size of Ni NPs on Al<sub>2</sub>O<sub>3</sub> is well controlled and maintained at ~5 nm irrespective of low- or high-temperature reduction. The formation of surface spinel species leads to a strong metal-support interaction and stabilizes the high dispersion of Ni NPs.<sup>122</sup>

The spatial distribution of the Ni nanoparticles has an effect as well.<sup>123,124</sup> Shen *et al.*<sup>123</sup> investigated the effect of micropores on the supported Ni/SiO<sub>2</sub> catalyst for CO<sub>2</sub> methanation. They found that there exist both ultra-small Ni nanoclusters and larger Ni nanoparticles for Ni/SiO<sub>2</sub> with plenty of micropores. However, only large Ni nanoparticles are present on the catalyst with fewer micropores. CO<sub>2</sub> can be activated to CO on small Ni nanoclusters during CO<sub>2</sub> methanation, and the generated CO will be further converted to methane on larger Ni nanoparticles.

The use of high surface area porous materials for highly dispersed Ni catalysts is always attractive. Haller and his co-workers<sup>125</sup> employed MCM-41 to load highly dispersed Ni nanoparticles on it for CO<sub>2</sub> methanation at temperatures as low as 573 K. At a Ni loading of 3 wt%, the methane selectivity reaches almost 100%. They confirmed that the hydrogen treatment of Ni-MCM-41 induces the formation of a highly dispersed and thermally stable metallic Ni catalyst. The highest activity and selectivity were achieved on the catalyst reduced at 973 K, with which Ni is mostly reduced to Ni<sup>0</sup> with a particle size of 1.7 nm. No serious aggregation was observed after the reaction

due to the surface anchoring effect.<sup>125</sup> Lu and his co-workers recently used metal–organic framework MOF-5 with a surface area of  $2961 \text{ m}^2 \text{ g}^{-1}$  to disperse Ni nanoparticles within it for  $\text{CO}_2$  methanation.<sup>126</sup> A very high dispersion of Ni (41.8%) has been achieved, leading to a significant enhanced activity.  $\text{CO}_2$  conversion reaches 47.2% at  $280^\circ\text{C}$  with a methane selectivity of 100% (from 200 to  $320^\circ\text{C}$ ). This MOF-5 supported Ni catalyst shows almost no deactivation in a long-term stability test up to 100 h.<sup>126</sup>

Chu and his co-workers<sup>127</sup> confirmed that the basic sites of the support have a significant effect on the activity of the Ni catalyst for  $\text{CO}_2$  methanation. This was also confirmed by Muroyama *et al.*<sup>128</sup> The treatment of the support can be applied towards the desired basic sites.<sup>127</sup>

The oxygen vacancy of the support significantly enhances the Ni–support interaction, stabilizes the nickel nanoparticles, promotes the formation of a Ni–support active interface and improves the adsorption of carbon dioxide and hydrogen.<sup>102,103,105,109,129–135</sup> Obviously, the effect of the support cannot be ignored.<sup>136,137</sup> Tsubaki and his co-workers<sup>138</sup> recently reported the preparation of nanoparticle promoted Ni-based bimodal pore catalysts by the impregnation of nickel precursor on  $\text{SiO}_2$ ,  $\text{Al}_2\text{O}_3$  and  $\text{ZrO}_2$  nanoparticle modified  $\text{SiO}_2$  supports. The catalysts were named Ni/ $\text{SiO}_2$ –Si, Ni/ $\text{SiO}_2$ –Al and Ni/ $\text{SiO}_2$ –Zr. The introduction of nanoparticles into the  $\text{SiO}_2$  support increases the surface area of the catalyst and improves the dispersion of nickel. The activity for  $\text{CO}_2$  methanation is significantly enhanced. The  $\text{CO}_2$  conversion increased in the order of Ni/ $\text{SiO}_2$  (unmodified catalyst) < Ni/ $\text{SiO}_2$ –Si < Ni/ $\text{SiO}_2$ –Al < Ni/ $\text{SiO}_2$ –Zr, corresponding to the increasing order of their surface areas. They found that the modification of  $\text{ZrO}_2$  and  $\text{Al}_2\text{O}_3$  nanoparticles improved  $\text{CO}_2$  chemisorption and dissociation, and thus resulted in extremely high  $\text{CH}_4$  selectivity (about 100%) at low reaction temperatures ( $<450^\circ\text{C}$ ).<sup>138</sup> A strong metal–support/promoter interaction was also observed in  $\text{ZrO}_2$  and  $\text{Al}_2\text{O}_3$  nanoparticle promoted catalysts, inhibiting the sintering of nickel and contributed to the high stabilities of these two catalysts in  $\text{CO}_2$  methanation.<sup>138</sup>

A strong Ni–support interaction is basically required to limit the catalyst size. Increasing investigations can be found in the use of a structured support for enhanced Ni–support interactions for  $\text{CO}_2$  methanation.<sup>139–152</sup> Catalysts with well-defined structures can lead to higher dispersion, better reactivity, improved selectivity and enhanced stability. In some cases, the structured catalyst itself contains nickel and acts as precursors. Since  $\text{CO}_2$  methanation is an exothermal reaction, the use of a structured catalyst not only improves the activity but also results in enhanced heat and mass transfer for optimum catalyst performance. Aziz *et al.*<sup>145</sup> prepared mesostructured silica nanoparticles (MSN) to obtain the Ni/MSN catalyst for  $\text{CO}_2$  methanation. They found that the catalytic performance of Ni/MSN closely depends on the structure of the catalyst, which consists of both intra- and inter-particle porosity. The presence of interparticle porosity facilitates the transport of reactant and product molecules during the reaction. The higher diffusion of  $\text{CO}_2$  in the pores of Ni/MSN increases overall reaction rates and results in higher conversion, compared to Ni/MCM-41. The

internal mass transfer resistance is negligible with this Ni/MSN catalyst. The high basicity of Ni/MSN catalysts is crucial to the high activity of the reaction with enhanced  $\text{CO}_2$  adsorption. The presence of defect sites or oxygen vacancies in MSN was considered to be responsible for the formation of surface carbon species, while Ni sites dissociate hydrogen into atomic hydrogen. Carbon atoms are then combined with atomic hydrogen for the formation of methane. The Ni/MSN catalyst shows good stability with no deactivation for 200 h.<sup>145</sup>

Borgschulte *et al.*<sup>146</sup> employed a nanostructured Ni@zeolite 5A catalyst for a sorption enhanced  $\text{CO}_2$  methanation with a methane yield up to 100%. Duan and his co-workers<sup>147</sup> applied a hierarchical  $\text{Al}_2\text{O}_3$  matrix for loading of high particle density nickel for  $\text{CO}_2$  methanation. A surface defect-promoted Ni catalyst with high dispersion is fabricated. It exhibits excellent activity and stability. Abundant surface vacancies generate and serve as active sites, resulting in significantly enhanced low-temperature activity. The anchoring effect from the support gives rise to high reaction stability, without sintering and/or aggregation of active species for long-term reactions.<sup>147</sup>

Li *et al.*<sup>148</sup> reported a Ni– $\text{Al}_2\text{O}_3$ /Ni-foam catalyst with enhanced heat transfer for  $\text{CO}_2$  methanation. This catalyst was prepared using a modified wet chemical etching method. A uniform NiO– $\text{Al}_2\text{O}_3$  composite catalyst layer ( $\sim 2 \mu\text{m}$ ) is efficiently formed and firmly anchored onto the foam structure by directly immersing the Ni-foam substrate into a chemical etching solution consisting of sodium dodecyl sulphate, acetic acid, and aluminum nitrate, followed by calcination under air. A high  $\text{CO}_2$  conversion of  $\sim 90\%$  with a high methane selectivity ( $>99.9\%$ ) has been obtained and remained stable for 1200 h.<sup>148</sup>

## 5. $\text{CO}_2$ hydrogenation to CO

According to Fig. 1, either direct  $\text{CO}_2$  dissociation or hydrogen-assisted  $\text{CO}_2$  dissociation can lead to the formation of CO. CO is an important intermediate for syntheses of methane and methanol.  $\text{CO}_2$  hydrogenation to CO or the RWGS reaction (reaction (5) in Table 1) is a side reaction of  $\text{CO}_2$  methanation and  $\text{CO}_2$  hydrogenation to methanol. Methane is normally the main product below  $600^\circ\text{C}$ .<sup>28</sup> A further increase in the reaction temperature causes CO formation.<sup>11,28,36,37</sup> 100% selectivity to CO can be observed at  $750^\circ\text{C}$ .<sup>28</sup> This suggests that the exothermic  $\text{CO}_2$  hydrogenation to methane dominates at temperatures below  $600^\circ\text{C}$ , whereas the RWGS reaction is the predominant one at temperatures above  $600^\circ\text{C}$ .<sup>28</sup>

As addressed above, the size of the nickel catalyst has a significant effect on the selectivity of  $\text{CO}_2$  hydrogenation, coupled with the support effect. The small catalyst size favours the selective hydrogenation of  $\text{CO}_2$  to CO. The  $\text{SiO}_2$  supported Ni catalyst has higher activity for RWGS, compared to  $\text{CeO}_2$  and  $\text{TiO}_2$ .<sup>36,120,153</sup> The Ni catalyst that adsorbs CO strongly favours  $\text{CO}_2$  hydrogenation to methane and methanol, while the catalyst that binds CO weakly tends to formation of CO.<sup>10,13</sup>

Lin *et al.*<sup>34</sup> reported a stable and active Ni/ $\gamma$ - $\text{Mo}_2\text{N}$  catalyst for the hydrogenation of  $\text{CO}_2$  to CO. They found that the pre-synthesized Ni particles of 4 nm are able to reverse sintering into the under-coordinated Ni species after a high temperature

activation procedure driven by the intense interaction between Ni and  $\gamma$ -Mo<sub>2</sub>N. The high dispersion of Ni occurs after the reduction of bulk phase Ni and the removal of the surface passivated O-layer of  $\gamma$ -Mo<sub>2</sub>N. The obtained Ni/ $\gamma$ -Mo<sub>2</sub>N catalyst shows 96% CO selectivity, at temperatures between 300 and 500 °C, with high CO<sub>2</sub> conversion.<sup>34</sup>

Based on the electronic configuration of the nickel atom, the Ni-SAC is excellent for CO<sub>2</sub> hydrogenation to CO. It was found that a single nickel atom is only able to take part in the 2e<sup>-</sup> redox cycle. Ni clusters are needed for the full hydrogenation of CO<sub>2</sub> with the 8e<sup>-</sup> redox cycle.<sup>35</sup> The unique characteristics of the SAC render Ni-SAC active for electro-chemical CO<sub>2</sub> reduction to CO.<sup>154–157</sup> Frei and his co-workers<sup>35</sup> confirmed that the MgO supported Ni-SAC is active for RWGS. MgO supported Ni NPs

are normally highly active for CO<sub>2</sub> methanation.<sup>158–160</sup> In<sub>2</sub>O<sub>3</sub> supported Ni-SACs were theoretically confirmed to be active for RWGS as well.<sup>29,161</sup> This can be further confirmed by the effect of the reaction temperature on the stability of the supported Ni-SAC.<sup>35</sup> It was reported that the MgO supported Ni-SAC remains stable at a reaction temperature of 300 °C, with which CO is produced through the RWGS reaction.<sup>35</sup> Particularly, the activity of the catalyst increases when the temperature increases from 200 °C to 300 °C, as shown in Fig. 9.<sup>35</sup> When the reaction temperature increases to 350 °C, methane and even methanol are produced with an aggregation of the Ni-SAC. As the reaction goes back to 300 °C, methane and methanol disappear. Only CO is detectable.<sup>35</sup> This obviously suggests that CO<sub>2</sub> hydrogenation

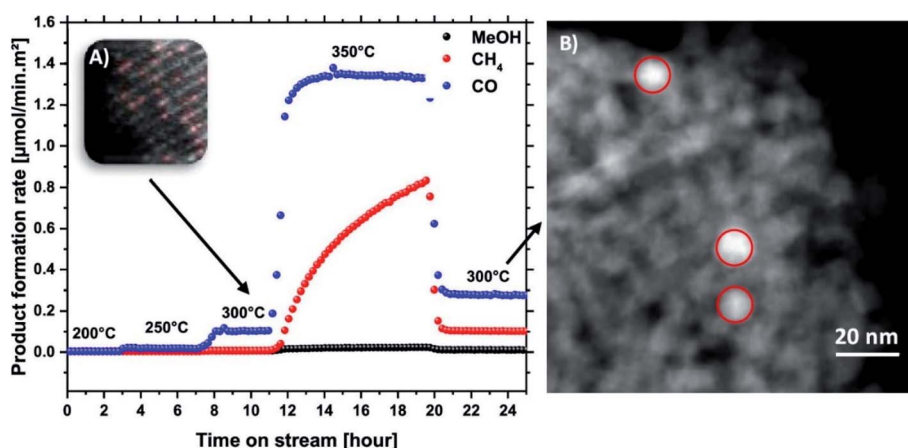


Fig. 9 (A) Product formation rate of Ni<sub>10</sub> at 30 bar, and different temperatures; the upper left corner represents the sample after 300 °C measurements. (B) TEM image of the sample after testing at 350 °C.<sup>35</sup> Copyright 2019, American Chemical Society.

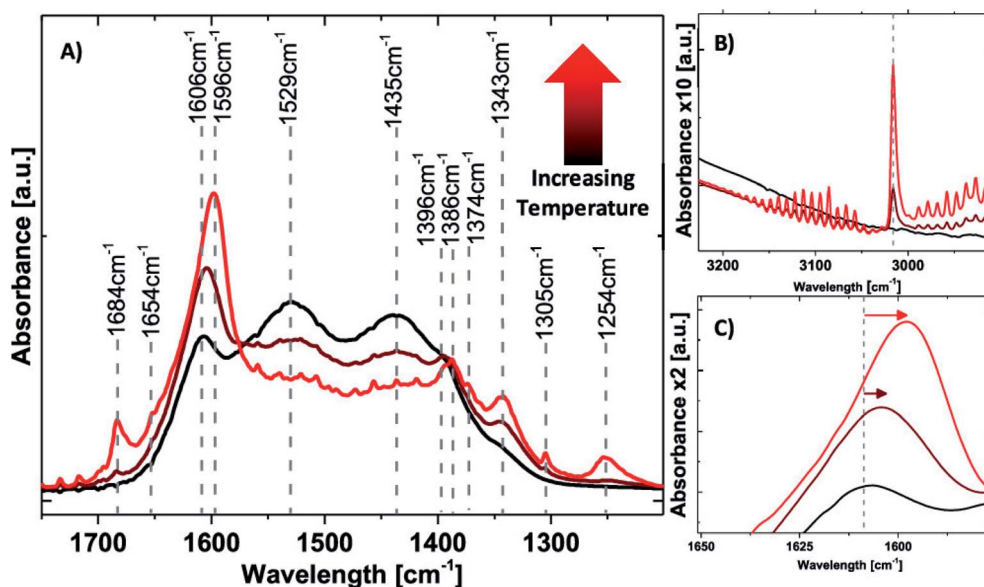


Fig. 10 IR spectroscopy under reaction conditions (4H<sub>2</sub>/CO<sub>2</sub>); stepwise increase from 200 °C (black), to 250 °C (dark red), and to 300 °C (red): (A) zoom-in of the 1200–1700 cm<sup>-1</sup> area; (B) zoom-in of the 2900–3200 cm<sup>-1</sup> area; (C) zoom-in of the 1550–1650 cm<sup>-1</sup> area.<sup>35</sup> Copyright 2019, American Chemical Society.



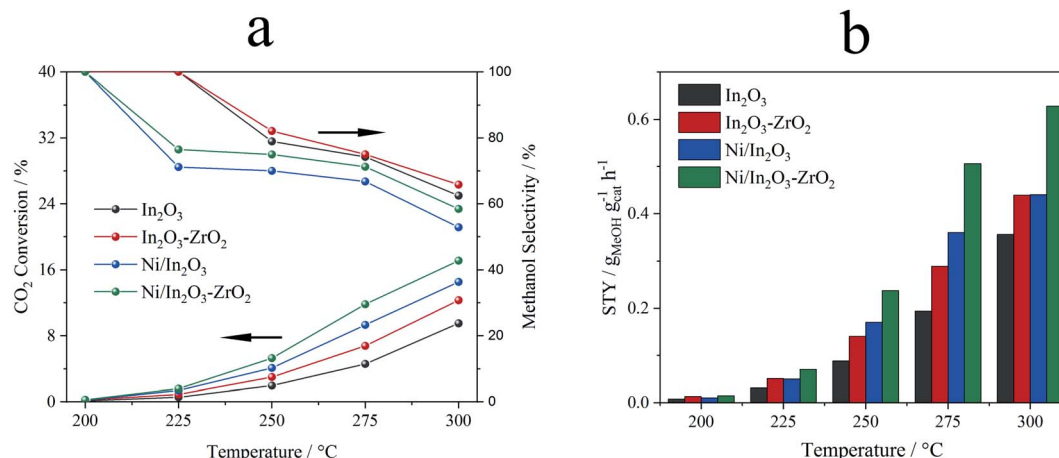


Fig. 11 Comparison of the activities of  $\text{Ni/In}_2\text{O}_3\text{-ZrO}_2$ ,  $\text{Ni/In}_2\text{O}_3$ ,  $\text{In}_2\text{O}_3\text{-ZrO}_2$  and  $\text{In}_2\text{O}_3$  for  $\text{CO}_2$  hydrogenation to methanol (5 wt% Ni loading). (a)  $\text{CO}_2$  conversion and methanol selectivity and (b) STY.<sup>31</sup> Copyright 2022, Elsevier.

to methane and methanol needs nickel clusters, not the Ni-SAC, with MgO as the support.<sup>35</sup>

*In situ* IR analyses were employed for  $\text{CO}_2$  hydrogenation over the MgO supported Ni-SAC.<sup>35</sup> As shown in Fig. 10, when the reaction temperature increases from 200 °C to 250 °C and then to 300 °C, a progressive decrease of the carbonate signals (1435, 1529  $\text{cm}^{-1}$ ) from the decomposition of the surface overlayer is observed, accompanied by an increase of the bicarbonate signal (1250  $\text{cm}^{-1}$ ), formate signals (1342, 1606  $\text{cm}^{-1}$ ), and the appearance of methane (Fig. 10A, 1305  $\text{cm}^{-1}$ ; Fig. 10B, 3016  $\text{cm}^{-1}$ ). This clearly shows that, with increasing temperatures, methane starts to form, evidence of the aggregates of the Ni-SAC. In addition, a pronounced shift in the formate area from 1607 to 1596  $\text{cm}^{-1}$  is observed, as shown in Fig. 10C. While values around 1600–1606  $\text{cm}^{-1}$  were assigned to formate species on MgO, values around 1591  $\text{cm}^{-1}$  were attributed to stretching vibrations from formate species on  $\text{Ni}^0$  nanoclusters, further supporting the correlation of cluster formation and methane production.<sup>35</sup>

A limitation with the use of Ni-SACs for the RWGS reaction is the possible formation of  $\text{Ni}(\text{CO})_4$ .<sup>162</sup> The Ni-SAC with intense Ni-support interactions is basically required for  $\text{CO}_2$  hydrogenation to avoid the formation of  $\text{Ni}(\text{CO})_4$ .

## 6. $\text{CO}_2$ hydrogenation to methanol

### 6.1 Theoretical studies

There is increasing interest in the use of supported nickel catalysts for  $\text{CO}_2$  hydrogenation to methanol. Fig. 1 shows that either direct  $\text{CO}_2$  dissociation or hydrogen-assisted  $\text{CO}_2$  dissociation can lead to methanol synthesis from  $\text{CO}_2$  hydrogenation. Three general pathways can be considered based on the mechanism of  $\text{CO}_2$  dissociation, including the formate pathway, CO hydrogenation pathway and RWGS pathway.<sup>10,22</sup> Peng *et al.*<sup>48</sup> predicted the possibility of  $\text{CO}_2$  hydrogenation to methanol on Ni (110). They found that Ni (110) takes the formate pathway for  $\text{CO}_2$  hydrogenation to methanol. However, two routes coexist *via*  $\text{HCOOH}^*$  and  $\text{H}_2\text{COO}^*$  species, as shown

in Fig. 1. The hydrogenation step of  $\text{CH}_2\text{O}^*$  to  $\text{CH}_3\text{O}^*$  competes with that to  $\text{CH}_2\text{OH}^*$ .<sup>48</sup> The hydrogenation of  $\text{CH}_3\text{O}^*$  to  $\text{CH}_3\text{OH}^*$  is the rate-determining step for the  $\text{CH}_3\text{O}$  route on Ni (110). They also found that the presence of  $\text{HCO}^*$  as a source of hydrogen facilitates the hydrogenation of  $\text{CH}_3\text{O}^*$ .<sup>48</sup> This suggests the promotional effect of CO. CO can also be involved in methanol synthesis.<sup>48</sup> CO can be first hydrogenated to  $\text{HCO}^*$ , which can be further hydrogenated to  $\text{CH}_2\text{O}^*$ , and finally to  $\text{CH}_3\text{OH}^*$  (through  $\text{CH}_3\text{O}^*$  or  $\text{CH}_2\text{OH}^*$ ).<sup>48</sup>

The formation of methanol from  $\text{CO}_2$  hydrogenation is theoretically feasible on  $\text{Ni}_{13}$ .<sup>50</sup> The optimized pathways for the formation of methanol and methane are  $\text{CO}_2^* \rightarrow \text{HCOO}^* \rightarrow \text{H}_2\text{COO}^* \rightarrow \text{H}_2\text{CO}^* \rightarrow \text{H}_3\text{CO}^* \rightarrow \text{CH}_3\text{OH}^*$  and  $\text{CO}_2^* \rightarrow \text{HCOO}^* \rightarrow \text{H}_2\text{COO}^* \rightarrow \text{H}_2\text{CO}^* \rightarrow \text{H}_3\text{CO}^* \rightarrow \text{CH}_3^* \rightarrow \text{CH}_4^*$ .<sup>50</sup> The hydrogenation or the dissociation of  $\text{H}_3\text{CO}^*$  determines the selectivity for  $\text{CH}_3\text{OH}$  and  $\text{CH}_4$ .<sup>50</sup>

The oxide support plays an important role in methanol synthesis from  $\text{CO}_2$  hydrogenation, as confirmed by our recent DFT study on  $\text{Ni}_4/\text{In}_2\text{O}_3$ .<sup>22</sup> It was shown that the RWGS pathway is the most theoretically-favoured for  $\text{CO}_2$  hydrogenation to methanol on  $\text{Ni}_4/\text{In}_2\text{O}_3$ .<sup>22</sup> The complete pathway follows  $\text{CO}_2^* \rightarrow \text{COOH}^* \rightarrow \text{CO}^* \rightarrow \text{HCO}^* \rightarrow \text{H}_2\text{CO}^* \rightarrow \text{H}_3\text{CO}^* \rightarrow \text{H}_3\text{COH}^*$ , as shown in Fig. 1. The interfacial oxygen vacancy of  $\text{In}_2\text{O}_3$  serves as the active site for boosting  $\text{CO}_2$  adsorption and charge transfer between nickel species and indium oxide, which synergistically promotes the consecutive  $\text{CO}_2$  hydrogenation towards methanol.<sup>22</sup> The dissociation of hydrogen occurs on Ni clusters in an almost barrier-less manner. The hydrogen adatoms spillover from the Ni cluster to the interfacial active site for the hydrogenation of adsorbed carbon dioxide. However, the nickel atom numbers have a big influence.  $\text{Ni}_1/\text{In}_2\text{O}_3$  and  $\text{Ni}_2/\text{In}_2\text{O}_3$  catalysts favour the RWGS reaction,<sup>29,161</sup> leading to CO formation, because of higher energy barriers for methanol synthesis.

The location of nickel in the support has an influence on the adsorption of carbon dioxide. The Ni atoms situated in the bulk do not significantly contribute to the conversion of carbon dioxide on the Ni-SAC catalyst on MgO.<sup>35</sup> Based on the DFT

calculations, as a nickel atom is located deeper in the subsurface, the contribution of Ni states to the bonding of adsorbed CO<sub>2</sub> species is decreased.<sup>35</sup> The location of the Ni-SAC on In<sub>2</sub>O<sub>3</sub> has significant effects on hydrogen dissociation as well for CO<sub>2</sub> hydrogenation.<sup>29</sup> For the stoichiometric In<sub>2</sub>O<sub>3</sub> surface and the In<sub>2</sub>O<sub>3</sub>(111) surface doped with a Ni single atom, H<sub>2</sub> dissociation leads to two OH groups. This indicates a homolytic dissociation.<sup>29</sup> The reaction over the stoichiometric surface is activated by 105 kJ mol<sup>-1</sup> with an adsorption energy ( $\Delta E_{\text{ads}}$ ) of -250 kJ mol<sup>-1</sup>. Doping of a Ni single atom in the In<sub>2</sub>O<sub>3</sub>(111) surface causes a small decrease of the activation barrier to 79 kJ mol<sup>-1</sup> with a more exothermic reaction energy ( $\Delta E_{\text{ads}}$  = -300 kJ mol<sup>-1</sup>).<sup>29</sup> If the Ni single atom is located on the In<sub>2</sub>O<sub>3</sub>(111) surface, instead of doping, H<sub>2</sub> activation involves the single Ni atom adsorbed on top of the In<sub>2</sub>O<sub>3</sub>(111) surface. One of the H atoms remains at the Ni atom, while the other migrates to a neighbouring O atom, resulting in, respectively, Ni-H and OH fragments.<sup>29</sup> The barrier associated with H<sub>2</sub> dissociation is only 11 kJ mol<sup>-1</sup>.<sup>29</sup> Similar results have been reported by Frei *et al.*<sup>161</sup> for Ni<sub>x</sub>-In<sub>2</sub>O<sub>3</sub> ensembles. Different from the Ni-SAC, H<sub>2</sub> activation over the In<sub>2</sub>O<sub>3</sub>(111) supported Ni<sub>8</sub> cluster occurs in two steps. After adsorption of molecular H<sub>2</sub> with  $\Delta E_{\text{ads}}$  of -90 kJ mol<sup>-1</sup>, H-H bond scission causes two H atoms to be adsorbed in a bridged configuration. With respect to the gas phase, the process of H<sub>2</sub> activation is barrier-less.<sup>29</sup> The same result has been also obtained on a defective In<sub>2</sub>O<sub>3</sub>(111) surface supported Ni<sub>4</sub> cluster<sup>22</sup> for CO<sub>2</sub> hydrogenation to methanol.

## 6.2 Experimental studies

A Ga<sub>2</sub>O<sub>3</sub> supported nickel catalyst was reported to be active for CO<sub>2</sub> hydrogenation to methanol.<sup>26</sup> A big size (10.2 nm) of the nickel catalyst shows the highest selectivity of methanol.<sup>26</sup> Smaller catalysts favour the RWGS reaction.<sup>26,163</sup> However, the mechanism is not clear. Further *operando* studies would be needed.

Jia *et al.*<sup>27</sup> employed wet chemical reduction to prepare the In<sub>2</sub>O<sub>3</sub> supported nickel catalyst with sodium borohydride (NaBH<sub>4</sub>) as a reducing agent. The obtained catalyst shows highly dispersed Ni species with intense Ni-In<sub>2</sub>O<sub>3</sub> interactions and enhanced oxygen vacancies. The highly dispersed Ni species serve as the active sites for hydrogen activation. Abundant H adatoms are thereby generated for oxygen vacancy creation on the In<sub>2</sub>O<sub>3</sub> surface. The enhanced surface oxygen vacancies further lead to improved CO<sub>2</sub> conversion. As a result, an effective synergy between the active Ni sites and surface oxygen vacancies on In<sub>2</sub>O<sub>3</sub> causes a high activity for CO<sub>2</sub> hydrogenation to methanol. The formation of methane can be ignored even at a nickel loading up to 10 wt%. When the reaction temperature is lower than 225 °C, the selectivity of methanol is 100%. It is higher than 64% in the temperature range between 225 °C and 275 °C. The methanol selectivity is still higher than 54% at 300 °C.<sup>27</sup> DFT calculations confirm that the electron transfer is partially from nickel to In<sub>2</sub>O<sub>3</sub>, similar to In<sub>2</sub>O<sub>3</sub> supported gold<sup>164</sup> and silver<sup>165</sup> catalysts for CO<sub>2</sub> hydrogenation to methanol. The intense Ni-In<sub>2</sub>O<sub>3</sub> interaction causes a big change in the pathway of CO<sub>2</sub> hydrogenation to methanol.

In<sub>2</sub>O<sub>3</sub> takes the formate pathway for methanol synthesis from CO<sub>2</sub> hydrogenation,<sup>166</sup> while the In<sub>2</sub>O<sub>3</sub> supported Ni<sub>4</sub> catalyst takes the RWGS pathway.<sup>22</sup> Catalyst characterization suggests that no InNi alloy is formed.<sup>27</sup> This was confirmed by Hensen and his co-workers with *operando* studies.<sup>29</sup> The Ni loading has a significant effect on the activity and selectivity of Ni/In<sub>2</sub>O<sub>3</sub> for CO<sub>2</sub> hydrogenation. A low Ni loading leads to the formation of Ni species in the form of single atoms or very small clusters.<sup>29</sup> These kinds of Ni species can significantly facilitate the dissociative adsorption of H<sub>2</sub>, which otherwise requires a high activation barrier on the pure In<sub>2</sub>O<sub>3</sub> surface.<sup>29</sup> The selective hydrogenation of CO<sub>2</sub> to methanol is thus caused. The formation of methane and CO was observed at high Ni loadings.<sup>29</sup>

The activity of Ni/In<sub>2</sub>O<sub>3</sub> for CO<sub>2</sub> hydrogenation to methanol can be further improved with the use of In<sub>2</sub>O<sub>3</sub>-ZrO<sub>2</sub> solid solution as the support.<sup>31</sup> A highly dispersed nickel catalyst is also obtained by chemical reduction.<sup>31</sup> A CO<sub>2</sub> conversion of 17.9% with a methanol yield of 0.63 gMeOH g<sub>cat</sub><sup>-1</sup> h<sup>-1</sup> was achieved at 300 °C and 5 MPa. Fig. 11 presents a comparison of the activities of In<sub>2</sub>O<sub>3</sub>, Ni/In<sub>2</sub>O<sub>3</sub> and Ni/In<sub>2</sub>O<sub>3</sub>-ZrO<sub>2</sub> with a Ni loading of 5 wt%.<sup>31</sup> A higher Ni loading results in the formation of methane, simultaneously with methanol synthesis from CO<sub>2</sub> hydrogenation.

## 7. Conclusions and outlook

From the investigations reported, the following conclusions can be made:

(1) The structure of the supported Ni catalyst has a significant effect on the adsorption and chemisorption of CO<sub>2</sub> on the catalyst surface, which will further affect the activity and selectivity of the catalyst.

(2) The structural controllable preparation of a supported nickel catalyst still remains a big challenge. The studies of the structural effect on CO<sub>2</sub> hydrogenation have mostly been *via* the size effect by far. A decrease in the size of a nickel catalyst causes an increase in the proportion of surface species, surface defects and heterogeneity of the atomic structure. The decreasing particle size enhances the quantum size effect with change in the electronic nature of the catalyst. This leads to improved hydrogen activation and enhanced Ni-support interactions, causing a change in the activity and selectivity for CO<sub>2</sub> hydrogenation. If the catalyst size goes down to a single nickel atom, the activity of the catalyst may undergo a total change because of the change in the electronic structure, induced by the quantum size effect.

(3) The supported Ni-SAC is generally a good catalyst for CO<sub>2</sub> hydrogenation to CO because of the electronic configuration of nickel and the electronic structure of the SAC. A support having intense interactions with the Ni-SAC is required for CO production in order to avoid the formation of Ni(CO)<sub>4</sub> at low reaction temperatures. The Ni-SAC shows high activity for CO<sub>2</sub> hydrogenation to methanol with In<sub>2</sub>O<sub>3</sub> as the support because of the strong Ni-In<sub>2</sub>O<sub>3</sub> interaction. The support has a significant effect on the properties of the supported Ni-SACs.

(4) The supported nickel nanoparticles are normally highly active for CO<sub>2</sub> hydrogenation to methane at temperatures below

600 °C. The selectivity of CO will reach 100% at temperatures above 750 °C. The reaction of CO<sub>2</sub> methanation has to compete with the side RWGS reaction. The structure of the supported nickel catalysts has a significant influence on the activity and selectivity for CO<sub>2</sub> methanation.

(5) With some specific supports, such as Ga<sub>2</sub>O<sub>3</sub>, In<sub>2</sub>O<sub>3</sub> and In<sub>2</sub>O<sub>3</sub>-ZrO<sub>2</sub>, the supported nickel catalyst becomes highly active towards CO<sub>2</sub> hydrogenation to methanol at temperatures below 350 °C. This big change is caused by the intense Ni-support interaction, which changes the electronic structure of the nickel catalyst and forms an active Ni-support interface for methanol synthesis from CO<sub>2</sub> hydrogenation. From the present understanding, it can be inferred that small nickel clusters are generally required for methanol synthesis from CO<sub>2</sub> hydrogenation. The DFT study confirms that the Ni/In<sub>2</sub>O<sub>3</sub> catalyst follows the RWGS pathway for CO<sub>2</sub> hydrogenation to methanol. The reaction of CO<sub>2</sub> hydrogenation to methanol has to compete with the side reactions of RWGS and CO<sub>2</sub> methanation.

(6) The theoretical studies suggested that CO<sub>2</sub> hydrogenation to formic acid is feasible over Ni-SACs with the support of unique electronic structures. Further experimental investigation is needed.

(7) Different CO<sub>2</sub> hydrogenation pathways will be induced by different catalyst structures. Considering the challenges in the structural analyses of the catalyst, the DFT is a very useful tool for studies of the catalyst structure, nickel-support interaction, conversion pathway and others.

(8) The theoretical and experimental studies confirmed that the oxygen vacancy and basic site of the support have significant effects on the activity and reaction mechanism of nickel catalysts for CO<sub>2</sub> hydrogenation. The strong interaction between nickel and the support helps to limit the nickel size for enhanced activity and to stabilize the catalytic activity. The intense interaction between nickel and In<sub>2</sub>O<sub>3</sub> with surface oxygen vacancies has made the catalyst highly active for CO<sub>2</sub> hydrogenation to methanol.

With the rapid development of renewable hydrogen technology, CO<sub>2</sub> hydrogenation over supported nickel catalysts attracts increasing interest worldwide. The innovation of supported nickel catalysts with a clear structure for CO<sub>2</sub> hydrogenation has become a big bottleneck. It is very necessary to conduct further fundamental studies in order to prepare nickel catalysts with controllable structures or better understand the structural effect on CO<sub>2</sub> hydrogenation. The following future studies are therefore suggested:

(1) Because of the complex network of CO<sub>2</sub> hydrogenation reactions, present theoretical studies have some obvious limitations. Even for the supported Ni-SAC with a well-defined structure, the reaction network is not simple. If the diffusion is further considered, the issue will be even more complex. Future studies have to consider the whole reaction network, although it is difficult at this moment. Big data technology will be useful for these important studies.

(2) The study of the supported Ni-SAC is just at the early stage. With the specific quantum size effect of the single nickel atom, we believe that the supported Ni-SAC will have more and more applications for CO<sub>2</sub> hydrogenation, encouraged by

extensive studies on the electro-chemical reduction of CO<sub>2</sub> by Ni-SACs and the studies of In<sub>2</sub>O<sub>3</sub> supported Ni-SACs. The investigation of supported Ni-SACs should focus on their unique properties for CO<sub>2</sub> hydrogenation and use them to tune the activity and selectivity.

(3) Further experimental studies are needed for CO<sub>2</sub> hydrogenation to formic acid over supported Ni-SAC catalysts. The key is to find a support that possesses unique interactions with Ni-SACs in order to stabilize the Ni-SAC, tune the electronic structure and overcome the thermodynamic obstacle.

(4) The development of *in situ* catalyst characterization technologies is immediately needed for the understanding of the structural effect of Ni catalysts. *Operando* FTIR analysis is still the most powerful tool at present for the *in situ* characterization of the catalyst for CO<sub>2</sub> hydrogenation. However, IR analyses are still limited for the measurement of species with weak signals. Innovation is needed for the IR measurements of chemical intermediates during CO<sub>2</sub> hydrogenation. NAP-XPS, STM and *operando* X-ray absorption spectroscopy have shown promising applications in the *in situ* characterization of Ni catalysts. More applications can be expected with these analyses with the development of atomic-scale observations of catalyst structures under real reaction conditions.

(5) The preparation of supported nickel catalysts with controllable structures has to be further investigated to meet the challenges in how to fabricate the desired catalyst and how to stabilize it during the reactions. This investigation should start from the very beginning of the shape and structure control of nickel nanocrystals with no supporting materials.

(6) The catalyst structure has a significant influence on CO<sub>2</sub> hydrogenation related reactions, including those with CO, methane, various chemical intermediates and, especially, carbon species formed during the reaction. There are many opportunities in these aspects. For example, if the nickel catalyst follows the CO pathway for CO<sub>2</sub> methanation, it must have good activity for CO methanation to obtain high activity for CO<sub>2</sub> methanation. One can learn information on CO methanation to develop promising catalysts for CO<sub>2</sub> methanation.

(7) The adsorbed CO species is an important intermediate for CO<sub>2</sub> hydrogenation over the supported nickel catalyst. It was confirmed that the catalyst that adsorbs CO strongly favors the formation of methane or methanol, while the one that binds CO weakly tends to produce carbon monoxide. CO can be a probe molecule for the *operando* study of nickel catalysts to understand the conversion pathway of CO<sub>2</sub> hydrogenation. Further progress can be expected.

(8) Because of the difficulty in structure identification, the present comparison of the properties of supported Ni catalysts for CO<sub>2</sub> hydrogenation may not be accurate. For example, if one would like to study the phase structure effect, it is better to compare the experimental data with the same catalyst size. And, if one would like to study the size effect, it is better to clearly fix the catalyst phase structure. Therefore, the structure analysis of the catalyst is basic. This is a key issue related to the supported nickel catalyst for CO<sub>2</sub> hydrogenation.

(9) Fundamental studies, including the nucleation and growth of the nickel crystal (especially on the porous supporting



materials), the interaction between the nickel and the support, the preparation of the supporting material with a clear porous structure and desired phase structure, are needed. Because of the importance of defects or oxygen vacancies on the support for CO<sub>2</sub> hydrogenation, the creation and the stability of such defects or vacancies are another significant challenge.

In summary, the studies of the structural effects of supported CO<sub>2</sub> hydrogenation are extremely important. Multidisciplinary efforts are needed. With advances in theoretical studies, data analyses, *operando* studies or *in situ* catalyst characterization, single atom catalyst and novel catalyst preparation, we believe further progress will be made soon for the practical applications of supported nickel catalysts for CO<sub>2</sub> hydrogenation.

## Conflicts of interest

There are no conflicts to declare.

## References

- J. Ding, Q. Liu, R.-P. Ye, W. Gong, F. Zhang, X. He, Y. Zhang, Q. Zhong, M. D. Argyle and M. Fan, *J. Mater. Chem. A*, 2021, **9**, 21877–21887.
- K. B. Tan, G. Zhan, D. Sun, J. Huang and Q. Li, *J. Mater. Chem. A*, 2021, **9**, 5197–5231.
- J. Zhang, C. D. Sewell, H. Huang and Z. Lin, *Adv. Energy Mater.*, 2021, **11**, 2102767.
- R.-P. Ye, J. Ding, W. Gong, M. D. Argyle, Q. Zhong, Y. Wang, C. K. Russell, Z. Xu, A. G. Russell, Q. Li, M. Fan and Y.-G. Yao, *Nat. Commun.*, 2019, **10**, 5698.
- Z. Yang, Y. Qi, F. Wang, Z. Han, Y. Jiang, H. Han, J. Liu, X. Zhang and W. J. Ong, *J. Mater. Chem. A*, 2020, **8**, 24868–24894.
- X.-Y. Meng, C. Peng, J. Jia, P. Liu, Y.-L. Men and Y.-X. Pan, *J. CO<sub>2</sub> Utiliz.*, 2022, **55**, 101844.
- Z.-J. Wang, H. Song, H. Liu and J. Ye, *Angew. Chem., Int. Ed.*, 2020, **59**, 8016.
- X. Su, J. Xu, B. Liang, H. Duan, B. Hou and Y. Huang, *J. Energy Chem.*, 2016, **25**, 553–565.
- B. Miao, S. S. K. Ma, X. Wang, H. Su and S. H. Chan, *Catal. Sci. Technol.*, 2016, **6**, 4048–4058.
- S. Kattel, P. Liu and J. G. Chen, *J. Am. Chem. Soc.*, 2017, **139**, 9739–9754.
- J. Ashok, S. Pati, P. Hongmanorom, Z. Tianxi, C. Junmei and S. Kawi, *Catal. Today*, 2020, **356**, 471–489.
- S. Rönisch, J. Schneider, S. Matthischke, M. Schlüter, M. Götz, J. Lefebvre, P. Prabhakaran and S. Bajohr, *Fuel*, 2016, **166**, 276–296.
- S. De, A. Dokania, A. Ramirez and J. Gascon, *ACS Catal.*, 2020, **10**, 14147–14185.
- X. Jiang, X. Nie, X. Guo, C. Song and J. G. Chen, *Chem. Rev.*, 2020, **120**, 7984–8034.
- Y. Wang, L. R. Winter, J. G. Chen and B. Yan, *Green Chem.*, 2021, **23**, 249–267.
- I. Hussain, A. A. Jalil, N. S. Hassan and M. Y. S. Hamid, *J. Energy Chem.*, 2021, **62**, 377–407.
- F. Sha, Z. Han, S. Tang, J. Wang and C. Li, *ChemSusChem*, 2020, **13**, 6160–6181.
- H.-Y. Kuang, Y.-X. Lin, X.-H. Li and J.-S. Chen, *J. Mater. Chem. A*, 2021, **9**, 20857–20873.
- P. Frontera, A. Macario, M. Ferraro and P. Antonucci, *Catalysts*, 2017, **7**, 59.
- Y. Li, S. H. Chan and Q. Sun, *Nanoscale*, 2015, **7**, 8663–8683.
- J.-B. Senderens and P. Sabatier, *Comptes Rendus Acad. Sci.*, 1902, **82**, 514–516.
- C. Shen, Q. Bao, W. Xue, K. Sun, Z. Zhang, X. Jia, D. Mei and C. Liu, *J. Energy Chem.*, 2022, **65**, 623–629.
- C. Vogt, M. Monai, G. J. Kramer and B. M. Weckhuysen, *Nat. Catal.*, 2019, **2**, 188–197.
- G. Yang, Y. Kuwahara, K. Mori, C. Louis and H. Yamashita, *Nano Res.*, 2021, DOI: 10.1007/s12274-021-3792-2.
- J. Zhang and Y. She, *Chin. J. Catal.*, 2020, **41**, 415–425.
- H. Choi, S. Oh, S. B. Trung Tran and J. Y. Park, *J. Catal.*, 2019, **376**, 68–76.
- X. Jia, K. Sun, J. Wang, C. Shen and C. Liu, *J. Energy Chem.*, 2020, **50**, 409–415.
- I. Sancho-Sanz, S. A. Korili and A. Gil, *Cat. Rev.*, 2021, DOI: 10.1080/01614940.2021.1968197.
- J. Zhu, F. Cannizzaro, L. Liu, H. Zhang, N. Kosinov, I. A. W. Filot, J. Rabeah, A. Brückner and E. J. M. Hensen, *ACS Catal.*, 2021, **11**, 11371–11384.
- N. H. M. Dostagir, C. Thompson, H. Kobayashi, A. M. Karim, A. Fukuoka and A. Shrotri, *Catal. Sci. Technol.*, 2020, **10**, 8196–8202.
- Z. Zhang, C. Shen, K. Sun and C. Liu, *Catal. Commun.*, 2022, **162**, 106386.
- X. Guo, H. Zhang, H. Yang, Z. Bo, J. Yan and K. Cen, *Sep. Purif. Technol.*, 2021, **279**, 119722.
- K. Homlamai, T. Maihom, S. Choomwattana, M. Sawangphruk and J. Limtrakul, *Appl. Surf. Sci.*, 2020, **499**, 143928.
- L. Lin, J. Liu, X. Liu, Z. Gao, N. Rui, S. Yao, F. Zhang, M. Wang, C. Liu, L. Han, F. Yang, S. Zhang, X.-d. Wen, S. D. Senanayake, Y. Wu, X. Li, J. A. Rodriguez and D. Ma, *Nat. Commun.*, 2021, **12**, 6978.
- M. Millet, G. Algara-Siller, S. Wrabetz, A. Mazheika, F. Girgsdies, D. Teschner, F. Seitz, A. Tarasov, S. V. Levchenko, R. Schlögl and E. Frei, *J. Am. Chem. Soc.*, 2019, **141**, 2451–2461.
- R. V. Gonçalves, L. L. R. Vono, R. Wojcieszak, C. S. B. Dias, H. Wender, E. Teixeira-Neto and L. M. Rossi, *Appl. Catal., B*, 2017, **209**, 240–246.
- Z. Zhang, X. Hu, Y. Wang, S. Hu, J. Xiang, C. Li, G. Chen, Q. Liu, T. Wei and D. Dong, *Fuel*, 2019, **237**, 566–579.
- A. Farjamnia and B. Jackson, *J. Chem. Phys.*, 2017, **146**, 74704.
- H. J. Freund and M. W. Roberts, *Surf. Sci. Rep.*, 1996, **25**, 225–273.
- S. Wang, D. Cao, Y. Li, J. Wang and H. Jiao, *J. Phys. Chem. B*, 2005, **109**, 18956–18963.
- D. Cao, Y. Li, J. Wang and H. Jiao, *Surf. Sci.*, 2009, **603**, 2991–2998.

- 42 R. C. Catapan, A. A. M. Oliveira, Y. Chen and D. G. Vlachos, *J. Phys. Chem. C*, 2012, **116**, 20281–20291.
- 43 M. Zhou, T. N. Le, L. K. Huynh and B. Liu, *Catal. Today*, 2017, **280**, 210–219.
- 44 H. Chen, M. Yang, J. Liu, G. Lu and X. Feng, *Catal. Sci. Technol.*, 2020, **10**, 5641–5647.
- 45 B. Kreitz, G. D. Wehinger, C. F. Goldsmith and T. Turek, *J. Phys. Chem. C*, 2021, **125**, 2984–3000.
- 46 G. Peng, S. J. Sibener, G. C. Schatz and M. Mavrikakis, *Surf. Sci.*, 2012, **606**, 1050–1055.
- 47 G. Peng, S. J. Sibener, G. C. Schatz, S. T. Ceyer and M. Mavrikakis, *J. Phys. Chem. C*, 2012, **116**, 3001–3006.
- 48 G. Peng, L. Xu, V. Glezakou and M. Mavrikakis, *Catal. Sci. Technol.*, 2021, **11**, 3279–3294.
- 49 A. L. Maulana, R. Putra, A. G. Saputro, M. K. Agusta, Nugraha and H. K. Dipojono, *Phys. Chem. Chem. Phys.*, 2019, **21**, 20276–20286.
- 50 P. Lozano-Reis, H. Prats, P. Gamallo, F. Illas and R. Sayós, *ACS Catal.*, 2020, **10**, 8077–8089.
- 51 Q. Ke, L. Kang, X. Chen and Y. Wu, *J. Chem. Sci.*, 2020, **132**, 151.
- 52 M. Silaghi, A. Comas-Vives and C. Copéret, *ACS Catal.*, 2016, **6**, 4501–4505.
- 53 A. Jafarzadeh, K. M. Bal, A. Bogaerts and E. C. Neyts, *J. Phys. Chem. C*, 2019, **123**, 6516–6525.
- 54 A. Cadi-Essadek, A. Roldan, X. Aparicio-Anglès and N. H. de Leeuw, *J. Phys. Chem. C*, 2018, **122**, 19463–19472.
- 55 K. R. Hahn, A. P. Seitsonen, M. Iannuzzi and J. Hutter, *ChemCatChem*, 2015, **7**, 625–634.
- 56 Y. Tang, Y. Wei, Z. Wang, S. Zhang, Y. Li, L. Nguyen, Y. Li, Y. Zhou, W. Shen, F. F. Tao and P. Hu, *J. Am. Chem. Soc.*, 2019, **141**, 7283–7293.
- 57 G. Alonso, E. López, F. Huarte-Larrañaga, R. Sayós, H. Prats and P. Gamallo, *J. CO<sub>2</sub> Utiliz.*, 2021, **54**, 101777.
- 58 K. Yuan, J. Zhong, X. Zhou, L. Xu, S. L. Bergman, K. Wu, G. Q. Xu, S. L. Bernasek, H. X. Li and W. Chen, *ACS Catal.*, 2016, **6**, 4330–4339.
- 59 S. Wang, D. Cao, Y. Li, J. Wang and H. Jiao, *J. Phys. Chem. B*, 2006, **110**, 9976–9983.
- 60 Y. Zhou, P. Lv and G. Wang, *J. Mol. Catal. A-Chem.*, 2006, **258**, 203–215.
- 61 I. N. Remediakis, F. Abild-Pedersen and J. K. Nørskov, *J. Phys. Chem. B*, 2004, **108**, 14535–14540.
- 62 S. J. Choe, H. J. Kang, S. Kim, S. Park, D. H. Park and D. S. Huh, *B. Korean Chem. Soc.*, 2005, **26**, 1682–1688.
- 63 C. Liu, T. R. Cundari and A. K. Wilson, *J. Phys. Chem. C*, 2012, **116**, 5681–5688.
- 64 P. Bothra, G. Periyasamy and S. K. Pati, *Phys. Chem. Chem. Phys.*, 2013, **15**, 5701.
- 65 H. S. Bengaard, J. K. Nørskov, J. Sehested, B. S. Clausen, L. P. Nielsen, A. M. Molenbroek and J. R. Rostrup-Nielsen, *J. Catal.*, 2002, **209**, 365–384.
- 66 J. A. Rodriguez, J. Evans, L. Feria, A. B. Vidal, P. Liu, K. Nakamura and F. Illas, *J. Catal.*, 2013, **307**, 162–169.
- 67 J. Ye, C. Liu, D. Mei and Q. Ge, *J. Catal.*, 2014, **317**, 44–53.
- 68 J. Ye, C. Liu, D. Mei and Q. Ge, *ACS Catal.*, 2013, **3**, 1296–1306.
- 69 L. C. Grabow and M. Mavrikakis, *ACS Catal.*, 2011, **1**, 365–384.
- 70 M. Huš, D. Kopač, N. S. Štefančič, D. L. Jurković, V. D. B. C. Dasireddy and B. Likozar, *Catal. Sci. Technol.*, 2017, **7**, 5900–5913.
- 71 N. Rui, K. Sun, C. Shen and C. Liu, *J. CO<sub>2</sub> Utiliz.*, 2020, **42**, 101313.
- 72 W. Lin, K. M. Stocker and G. C. Schatz, *J. Am. Chem. Soc.*, 2017, **139**, 4663–4666.
- 73 X. Nie, H. Wang, W. Li, Y. Chen, X. Guo and C. Song, *J. CO<sub>2</sub> Util.*, 2018, **24**, 99–111.
- 74 P. Frontera, A. Macario, G. Monforte, G. Bonura, M. Ferraro, G. Dispenza, V. Antonucci, A. S. Aricò and P. L. Antonucci, *Int. J. Hydrogen Energy*, 2017, **42**, 26828–26842.
- 75 G. Varvoutis, M. Lykaki, S. Stefa, V. Binas, G. E. Marnellos and M. Konsolakis, *Appl. Catal., B*, 2021, **297**, 120401.
- 76 J. W. Hu, P. Hongmanorom, P. Chirawatkul and S. Kawi, *Chem. Eng. J.*, 2021, **426**, 130864.
- 77 S. Tada, T. Shimizu, H. Kameyama, T. Haneda and R. Kikuchi, *Int. J. Hydrogen Energy*, 2012, **37**, 5527–5531.
- 78 H. Liu, X. Zou, X. Wang, X. Lu and W. Ding, *J. Nat. Gas Chem.*, 2012, **21**, 703–707.
- 79 H. Chen, *J. Phys. Chem. C*, 2012, **116**, 6239–6246.
- 80 M. Huang and S. Fabris, *J. Phys. Chem. C*, 2008, **112**, 8643–8648.
- 81 Y. Song, L. Yin, J. Zhang, P. Hu, X. Gong and G. Lu, *Surf. Sci.*, 2013, **618**, 140–147.
- 82 M. Roiaz, E. Monachino, C. Dri, M. Greiner, A. Knop-Gericke, R. Schlögl, G. Comelli and E. Vesselli, *J. Am. Chem. Soc.*, 2016, **138**, 4146–4154.
- 83 C. Heine, B. A. J. Lechner, H. Bluhm and M. Salmeron, *J. Am. Chem. Soc.*, 2016, **138**, 13246–13252.
- 84 Q. Wang, L. Wei, M. Sullivan, S. Yang and Y. Chen, *RSC Adv.*, 2013, **3**, 3046–3053.
- 85 J. Lahiri, T. Miller, L. Adamska, I. I. Oleynik and M. Batzill, *Nano Lett.*, 2011, **11**, 518–522.
- 86 Y. Gamo, A. Nagashima, M. Wakabayashi, M. Terai and C. Oshima, *Surf. Sci.*, 1997, **374**, 61–64.
- 87 Z. Fan, K. Sun, N. Rui, B. Zhao and C. Liu, *J. Energy Chem.*, 2015, **24**, 655–659.
- 88 R. Zhou, N. Rui, Z. Fan and C. Liu, *Int. J. Hydrogen Energy*, 2016, **41**, 22017–22025.
- 89 Z. Wang, X. M. Cao, J. Zhu and P. Hu, *J. Catal.*, 2014, **311**, 469–480.
- 90 A. Ambrosetti and P. L. Silvestrelli, *J. Chem. Phys.*, 2016, **144**, 111101.
- 91 L. L. Patera, F. Bianchini, G. Troiano, C. Dri, C. Cepek, M. Peressi, C. Africh and G. Comelli, *Nano Lett.*, 2015, **15**, 56–62.
- 92 X. Zhang, L. Wang, J. Xin, B. I. Yakobson and F. Ding, *J. Am. Chem. Soc.*, 2014, **136**, 3040–3047.
- 93 F. Bianchini, L. L. Patera, M. Peressi, C. Africh and G. Comelli, *J. Phys. Chem. Lett.*, 2014, **5**, 467–473.
- 94 L. L. Patera, F. Bianchini, C. Africh, C. Dri, G. Soldano, M. M. Mariscal, M. Peressi and G. Comelli, *Science*, 2018, **359**, 1243–1246.

- 95 M. Wei, Q. Fu, Y. Yang, W. Wei, E. Crumlin, H. Bluhm and X. Bao, *J. Phys. Chem. C*, 2015, **119**, 13590–13597.
- 96 C. Vogt, E. Groeneveld, G. Kamsma, M. Nachtegaal, L. Lu, C. J. Kiely, P. H. Berben, F. Meirer and B. M. Weckhuysen, *Nat. Catal.*, 2018, **1**, 127–134.
- 97 B. Mutz, H. W. P. Carvalho, S. Mangold, W. Kleist and J. Grunwaldt, *J. Catal.*, 2015, **327**, 48–53.
- 98 K. Feng, J. Tian, M. Guo, Y. Wang, S. Wang, Z. Wu, J. Zhang, L. He and B. Yan, *Appl. Catal., B*, 2021, **292**, 120191.
- 99 Z. Hao, J. Shen, S. Lin, X. Han, X. Chang, J. Liu, M. Li and X. Ma, *Appl. Catal., B*, 2021, **286**, 119922.
- 100 Z. Yan, Q. Liu, L. Liang and J. Ouyang, *J. CO<sub>2</sub> Util.*, 2021, **47**, 101489.
- 101 N. A. Sholeha, S. Mohamad, H. Bahruji, D. Prasetyoko, N. Widiastuti, N. A. Abdul Fatah, A. A. Jalil and Y. H. Taufiq-Yap, *RSC Adv.*, 2021, **11**, 16376–16387.
- 102 X. Jia, X. Zhang, N. Rui, X. Hu and C. Liu, *Appl. Catal., B*, 2019, **244**, 159–169.
- 103 N. Rui, X. Zhang, F. Zhang, Z. Liu, X. Cao, Z. Xie, R. Zou, S. D. Senanayake, Y. Yang, J. A. Rodriguez and C. Liu, *Appl. Catal., B*, 2021, **282**, 119581.
- 104 Y. Li, Y. Men, S. Liu, J. Wang, K. Wang, Y. Tang, W. An, X. Pan and L. Li, *Appl. Catal., B*, 2021, **293**, 120206.
- 105 Y. Du, C. Qin, Y. Xu, D. Xu, J. Bai, G. Ma and M. Ding, *Chem. Eng. J.*, 2021, **418**, 129402.
- 106 P. Hongmanorom, J. Ashok, P. Chirawatkul and S. Kawi, *Appl. Catal., B*, 2021, **297**, 120454.
- 107 M. Liu, H. Chen, C. Chen, J. Wu, H. Wu and C. Yang, *Nanoscale*, 2019, **11**, 20741–20753.
- 108 X. Xu, Y. Tong, J. Huang, J. Zhu, X. Fang, J. Xu and X. Wang, *Fuel*, 2021, **283**, 118867.
- 109 S. Tada, H. Nagase, N. Fujiwara and R. Kikuchi, *Energ. Fuel.*, 2021, **35**, 5241–5251.
- 110 J. Ren, H. Guo, J. Yang, Z. Qin, J. Lin and Z. Li, *Appl. Surf. Sci.*, 2015, **351**, 504–516.
- 111 X. Yan, Y. Liu, B. Zhao, Z. Wang, Y. Wang and C. Liu, *Int. J. Hydrogen Energy*, 2013, **38**, 2283–2291.
- 112 X. Zhu, P. Huo, Y. Zhang, D. Cheng and C. Liu, *Appl. Catal., B*, 2008, **81**, 132–140.
- 113 Y. Dai, R. Zou, T. Ba, J. Zhang and C. Liu, *J. CO<sub>2</sub> Util.*, 2021, **51**, 101647.
- 114 J. Zhang, X. Jia and C. Liu, *RSC Adv.*, 2022, **12**, 721–727.
- 115 P. Lan, C. Wang and C. Chen, *J. Taiwan Inst. Chem. E.*, 2020, **116**, 188–196.
- 116 L. Liu, S. Wang, Y. Guo, B. Wang, P. Rukundo, S. Wen and Z. Wang, *Int. J. Hydrogen Energy*, 2016, **41**, 17361–17369.
- 117 J. Liu, W. Bing, X. Xue, F. Wang, B. Wang, S. He, Y. Zhang and M. Wei, *Catal. Sci. Technol.*, 2016, **6**, 3976–3983.
- 118 X. Li, D. Li, H. Tian, L. Zeng, Z. Zhao and J. Gong, *Appl. Catal., B*, 2017, **202**, 683–694.
- 119 F. Yang, D. Deng, X. Pan, Q. Fu and X. Bao, *Natl. Sci. Rev.*, 2015, **2**, 183–201.
- 120 K. Wang, Y. Men, S. Liu, J. Wang, Y. Li, Y. Tang, Z. Li, W. An, X. Pan and L. Li, *Fuel*, 2021, **304**, 121388.
- 121 C. Vogt, M. Monai, E. B. Sterk, J. Palle, A. E. M. Melcherts, B. Zijlstra, E. Groeneveld, P. H. Berben, J. M. Boereboom, E. J. M. Hensen, F. Meirer, I. A. W. Filot and B. M. Weckhuysen, *Nat. Commun.*, 2019, **10**, 5330.
- 122 S. Li, Q. Wang, J. Lu, X. Deng, S. Bi, Z. Song, C. Guo, R. Li and X. Yan, *Cryst. Eng. Comm.*, 2019, **21**, 6709–6718.
- 123 L. Shen, M. Zhu and J. Xu, *Greenhouse Gas. Sci. Technol.*, 2021, **11**, 1213–1221.
- 124 D. Beierlein, D. Häussermann, M. Pfeifer, T. Schwarz, K. Stöwe, Y. Traa and E. Klemm, *Appl. Catal., B*, 2019, **247**, 200–219.
- 125 G. Du, S. Lim, Y. Yang, C. Wang, L. Pfefferle and G. L. Haller, *J. Catal.*, 2007, **249**, 370–379.
- 126 W. Zhen, B. Li, G. Lu and J. Ma, *Chem. Commun.*, 2015, **51**, 1728–1731.
- 127 M. Chen, Z. Guo, J. Zheng, F. Jing and W. Chu, *J. Energy Chem.*, 2016, **25**, 1070–1077.
- 128 H. Muroyama, Y. Tsuda, T. Asakoshi, H. Masitah, T. Okanishi, T. Matsui and K. Eguchi, *J. Catal.*, 2016, **343**, 178–184.
- 129 P. Unwiset, K. C. Chanapattarapol, P. Kidkhunthod, Y. Poornorn and B. Ohtani, *Chem. Eng. Sci.*, 2020, **228**, 115955.
- 130 Y. Quan, N. Zhang, Z. Zhang, Y. Han, J. Zhao and J. Ren, *Int. J. Hydrogen Energy*, 2021, **46**, 14395–14406.
- 131 M. Zhu, P. Tian, X. Cao, J. Chen, T. Pu, B. Shi, J. Xu, J. Moon, Z. Wu and Y. Han, *Appl. Catal., B*, 2021, **282**, 119561.
- 132 G. I. Siakavelas, N. D. Charisiou, S. Alkhoori, A. A. Alkhoori, V. Sebastian, S. J. Hinder, M. A. Baker, I. V. Yentekakis, K. Polychronopoulou and M. A. Goula, *Appl. Catal., B*, 2021, **282**, 119562.
- 133 Y. Zhang, T. Zhang, F. Wang, Q. Zhu and Q. Liu, *Greenhouse Gas. Sci. Technol.*, 2021, **11**, 1222–1233.
- 134 S. Lin, Z. Hao, J. Shen, X. Chang, S. Huang, M. Li and X. Ma, *J. Energy Chem.*, 2021, **59**, 334–342.
- 135 R. Tang, N. Ullah, Y. Hui, X. Li and Z. Li, *Mol. Catal.*, 2021, **508**, 111602.
- 136 P. Strucks, L. Failing and S. Kaluza, *Chem.-Ing.-Tech.*, 2021, **93**, 1–12.
- 137 L. Shen, J. Xu, M. Zhu and Y. Han, *ACS Catal.*, 2020, **10**, 14581–14591.
- 138 P. Zhu, Q. Chen, Y. Yoneyama and N. Tsubaki, *RSC Adv.*, 2014, **4**, 64617–64624.
- 139 X. Fang, L. Xia, S. Li, Z. Hong, M. Yang, X. Xu, J. Xu and X. Wang, *Fuel*, 2021, **293**, 120460.
- 140 H. S. Lim, G. Kim, Y. Kim, M. Lee, D. Kang, H. Lee and J. W. Lee, *Chem. Eng. J.*, 2021, **412**, 127557.
- 141 H. Tian, X. Li, L. Zeng and J. Gong, *ACS Catal.*, 2015, **5**, 4959–4977.
- 142 J. Zhang and F. Li, *Appl. Catal., B*, 2015, **176–177**, 513–521.
- 143 L. Xu, Z. Miao, H. Song, W. Chen and L. Chou, *Catal. Sci. Technol.*, 2014, **4**, 1759–1770.
- 144 Z. Li, L. Mo, Y. Kathiraser and S. Kawi, *ACS Catal.*, 2014, **4**, 1526–1536.
- 145 M. A. A. Aziz, A. A. Jalil, S. Triwahyono, R. R. Mukti, Y. H. Taufiq-Yap and M. R. Sazegar, *Appl. Catal., B*, 2014, **147**, 359–368.
- 146 A. Borgschulte, N. Gallandat, B. Probst, R. Suter, E. Callini, D. Ferri, Y. Arroyo, R. Erni, H. Geerlings and A. Züttel, *Phys. Chem. Chem. Phys.*, 2013, **15**, 9620–9625.



- 147 S. He, C. Li, H. Chen, D. Su, B. Zhang, X. Cao, B. Wang, M. Wei, D. G. Evans and X. Duan, *Chem. Mater.*, 2013, **25**, 1040–1046.
- 148 Y. Li, Q. Zhang, R. Chai, G. Zhao, Y. Liu, Y. Lu and F. Cao, *AIChE J.*, 2015, **61**, 4323–4331.
- 149 A. Vita, C. Italiano, L. Pino, P. Frontera, M. Ferraro and V. Antonucci, *Appl. Catal., B*, 2018, **226**, 384–395.
- 150 L. Xu, F. Wang, M. Chen, D. Nie, X. Lian, Z. Lu, H. Chen, K. Zhang and P. Ge, *Int. J. Hydrogen Energy*, 2017, **42**, 15523–15539.
- 151 G. Zhou, H. Liu, K. Cui, H. Xie, Z. Jiao, G. Zhang, K. Xiong and X. Zheng, *Int. J. Hydrogen Energy*, 2017, **42**, 16108–16117.
- 152 Q. Zhang, R. Xu, N. Liu, C. Dai, G. Yu, N. Wang and B. Chen, *Appl. Surf. Sci.*, 2022, **579**, 152204.
- 153 M. Li, H. Amari and A. C. van Veen, *Appl. Catal., B*, 2018, **239**, 27–35.
- 154 J. Zhang, H. Zhang, Y. Wu, C. Liu, Y. Huang, W. Zhou and B. Zhang, *J. Mater. Chem. A*, 2022, DOI: 10.1039/d1ta07910g.
- 155 Y. Huang, F. Rehman, M. Tamtaji, X. Li, Y. Huang, T. Zhang and Z. Luo, *J. Mater. Chem. A*, 2022, DOI: 10.1039/d1ta08337f.
- 156 L. Wang, W. Chen, D. Zhang, Y. Du, R. Amal, S. Qiao, J. Wu and Z. Yin, *Chem. Soc. Rev.*, 2019, **48**, 5310–5349.
- 157 T. Cui, L. Li, C. Ye, X. Li, C. Liu, S. Zhu, W. Chen and D. Wang, *Adv. Funct. Mater.*, 2021, 2108381.
- 158 J. Huang, X. Li, X. Wang, X. Fang, H. Wang and X. Xu, *J. CO<sub>2</sub> Utiliz.*, 2019, **33**, 55–63.
- 159 G. Baldauf-Sommerbauer, S. Lux, W. Aniser, B. Bitschnau, I. Letofsky-Papst and M. Siebenhofer, *J. CO<sub>2</sub> Utiliz.*, 2018, **23**, 1–9.
- 160 W. K. Fan and M. Tahir, *J. Environ. Chem. Eng.*, 2021, **9**, 105460.
- 161 M. S. Frei, C. Mondelli, R. Garcia-Muelas, J. Morales-Vidal, M. Philipp, O. V. Safonova, N. Lopez, J. A. Stewart, D. C. Ferre and J. Perez-Ramirez, *Nat. Commun.*, 2021, **12**, 1960.
- 162 A. M. Abdel-Mageed and S. Wohlrab, *Catalysts*, 2022, **12**, 16.
- 163 J. Gong, M. Chu, W. Guan, Y. Liu, Q. Zhong, M. Cao and Y. Xu, *Ind. Eng. Chem. Res.*, 2021, **60**, 9448–9455.
- 164 N. Rui, F. Zhang, K. Sun, Z. Liu, W. Xu, E. Stavitski, S. D. Senanayake, J. A. Rodriguez and C. Liu, *ACS Catal.*, 2020, **10**, 11307–11317.
- 165 K. Sun, Z. Zhang, C. Shen, N. Rui and C. Liu, *Green Energy Environ.*, 2021, DOI: 10.1016/j.gee.2021.05.004.
- 166 J. Ye, C. Liu, D. Mei and Q. Ge, *ACS Catal.*, 2013, **3**, 1296–1306.